

Nanoparticles Incorporating a Fluorescence Turn-on Reporter for Real-Time Drug Release Monitoring, a Chemoenhancer and a Stealth Agent: Poseidon's Trident against Cancer?

Arjun Attri, Deepak Thakur, Taranpreet Kaur, Sebastian Sensale, Zhangli Peng, Deepak Kumar, and Raman Preet Singh*



Cite This: *Mol. Pharmaceutics* 2021, 18, 124–147



Read Online

ACCESS |



Metrics & More



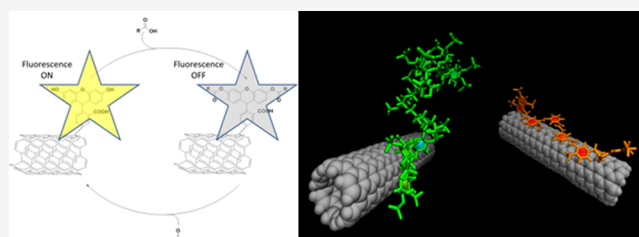
Article Recommendations



Supporting Information

ABSTRACT: The rate and extent of drug release under physiological conditions is a key factor influencing the therapeutic activity of a formulation. Real-time detection of drug release by conventional pharmacokinetics approaches is confounded by low sensitivity, particularly in the case of tissue-targeted novel drug delivery systems, where low concentrations of the drug reach systemic circulation. We present a novel fluorescence turn-on platform for real-time monitoring of drug release from nanoparticles based on reversible fluorescence quenching in fluorescein esters. Fluorescein-conjugated carbon nanotubes (CNTs) were esterified with methotrexate in solution and solid phase, followed by supramolecular functionalization with a chemoenhancer (suramin) or/and a stealth agent (dextran sulfate). Suramin was found to increase the cytotoxicity of methotrexate in A549 cells. On the other hand, dextran sulfate exhibited no effect on cytotoxicity or cellular uptake of CNTs by A549 cells, while a decrease in cellular uptake of CNTs and cytotoxicity of methotrexate was observed in macrophages (RAW 264.7 cells). Similar results were also obtained when CNTs were replaced with graphene. Docking studies revealed that the conjugates are not internalized by folate receptors/transporters. Further, docking and molecular dynamics studies revealed the conjugates do not exhibit affinity toward the methotrexate target, dihydrofolate reductase. Molecular dynamics studies also revealed that distinct features of dextran-CNT and suramin-CNT interactions, characterized by π - π interactions between CNTs and dextran/suramin. Our study provides a simple, cost-effective, and scalable method for the synthesis of nanoparticles conferred with the ability to monitor drug release in real-time. This method could also be extended to other drugs and other types of nanoparticles.

KEYWORDS: fluorescence, nanoparticles, real-time drug release, carbon nanotubes



INTRODUCTION

The field of novel drug delivery systems has never witnessed a phase, as today, with new delivery systems being developed to achieve higher efficacy, reduced toxicity, and targeted delivery. As new formulations are developed, it becomes imperative to predict their behavior following their interaction with cells. One of the key factors that can alter the performance of a formulation is the drug release under physiological conditions. An *in vitro* drug release profile in the dissolution medium of various pH and ionic strengths, simulating various cellular/body compartments, is currently employed to predict formulation behavior in these compartments. However, such *in vitro* studies could not accurately predict the drug release profile in biological compartments as the simulated medium are devoid of the complex pool of biomolecules present in biological systems that can alter the release profile.^{1–3}

Novel drug delivery systems present a more technical challenging situation as compared to conventional formulations because of sustained drug release from the former.^{2,4} This

leads to low drug concentrations during the initial time periods, which may be beyond the detection limit of instruments or the drug signal may be lost in the high background noise of biological samples. These technical challenges prevent real-time detection of drug release during the initial periods. Some studies have attempted to employ fluorescence-based methods for determining drug release from formulation. One of these methods relies on fluorescence activation following release, and subsequent activation, of nonfluorescent prodrugs or drug conjugates.^{5–7} Recently, more intricate systems employing fluorophore pairs, fluorophore-quencher pairs, and other approaches have also been

Received: July 13, 2020

Revised: November 13, 2020

Accepted: November 16, 2020

Published: December 21, 2020



employed.^{8,9} However, a basic limitation in these studies was that these reported systems generally employed either fluorescent drugs^{8,10,11} or fluorescent dyes^{12–16} as model molecules thereby limiting the applicability of the formulation to a single or a very narrow range of compounds.^{17,18}

The novel drug delivery systems, particularly particulate systems like nanoparticles (NPs), pose another challenge: accumulation in organs of the reticuloendothelial system (RES) such as the liver, lungs, and spleen. As a result of this, the effective drug concentration available at the target site is reduced along with a significant increase in drug concentration at nontarget sites (RES organs), potentially leading to a decrease in therapeutic activity with a concomitant increase in toxicity at nontarget sites.¹⁹

The evasion of RES uptake has been successfully attempted using ligands like polyethylene glycol (PEG) or its derivatives. However, PEG could potentially interfere with the conjugation of other ligands and drugs due to steric factors arising from its long chain length. Apart from PEG, there are few other ligands that could effectively evade RES, thereby limiting the available arsenal for RES evasion.¹⁹ In a previous study, we found that macrophages, which are major cells responsible for NP uptake by RES organs, internalize NPs as a function of surface charge. The cellular uptake of multiwalled carbon nanotubes (MWCNTs) was found to be dependent on scavenger receptors (SRs) and inhibited by SR inhibitor, dextran sulfate (DS); the degree of cellular uptake of MWCNTs in the presence of DS was comparable to that of PEG-functionalized MWCNTs.²⁰ Around the same time, another report appeared whereby the authors have shown by fluorescence microscopy that DS-coated and PEG-coated single-walled carbon nanotubes are not internalized by macrophages due to evasion of opsonin binding.²¹ In another study, coadministration of DS resulted in reduced accumulation of superparamagnetic iron oxide NPs in RES organs.²² Hence, these studies suggest that DS is an attractive stealth ligand that has not been systematically and extensively explored for drug delivery purposes.

A probable alternate approach to RES evasion is to include synergistic mixtures that show high activity at the target site but not at nontarget sites. Chemoenhancers are a class of compounds that can potentially increase the anticancer activity of chemotherapeutic agents. Low dose suramin (SU) has been proposed as a chemoenhancer in cancer chemotherapy and acts via multiple pathways such as inhibition of fibroblast growth factor,²³ epidermal growth factor,²⁴ Wnt,^{25,26} G-protein,^{25,27} and STATs signaling.²⁸ SU also inhibits ATP-induced cell proliferation²⁹ and inhibits HuR³⁰ and telomerase.³¹ All of these mechanisms contribute to inhibition of angiogenesis³² and decrease in tissue invasion and metastasis,^{29,30} resulting in tumor regression in animal models.³¹ Further, the combination of SU with drugs has been shown to enhance the activity of anticancer drugs in animal models^{33,34} and in Phase I, II, and III clinical trials.³⁵ Despite the fact that SU inhibits several mechanisms upregulated in tumors and the success of SU–anticancer drug combinations in clinical trials, novel drug delivery systems combining SU with anticancer drugs have not received attention. A nanogel containing doxorubicin–SU combination³⁴ has been reported to be effective in a lung metastasis model whereby SU was used as a chemoenhancer. Apart from this, SU has been employed as a polyanion for formulation purposes such as heparin–suramin conjugate for the formulation of nanocomplexes of poly-

ethylene-glycol-protamine for tumor delivery,³⁶ where the heparin–suramin complex was selected based on its ability to provide an optimal particle size to the nanocomplex. Additionally, SU has also been encapsulated in nanoparticles of an alendronate-conjugated bone-targeted polymer or treatment of fibrous dysplasia.³⁷

The present study was conducted to develop a system that can be used as platform technology for real-time drug release monitoring. We developed a carbon nanotube (CNT)-based system to determine the release rate of covalently linked drugs. Additionally, the possibility of employing a chemoenhancer (SU) and a stealth agent (DS) are explored. CNTs were chosen as a model delivery system for several reasons: (1) CNTs are a versatile platform that can be used to attach a wide range of chemical moieties; (2) the CNT backbone is not degraded intracellularly, while the attached molecules are released by cleavage of covalent linkages; (3) CNTs can be easily separated from the released drug. It is pertinent to mention here that, although CNTs have been used as a model NP, the approach can be extended to other nanoparticles as well. Methotrexate (MET) is a commonly used antineoplastic drug approved for use in multiple types of cancers. Further, MET is chemically stable and contains carboxylic groups, which could be easily esterified with fluorescein. Therefore, MET was chosen as a model compound for the present study.

MATERIALS AND METHODS

Chemicals and Drugs. Bovine serum albumin (BSA), 3,3'-diaminobenzidine (DAB), dichlorotriazinylamino fluorescein (DTAF), fluorescein isothiocyanate (FITC), 3-(4,5-dimethylthiazol-2-yl)-2,5-diphenyltetrazolium bromide (MTT), rhodamine B isothiocyanate (RBITC), Tween-20, 24-well transwell inserts, and culture medium components were purchased from HiMedia, India. Aspirin, dimethylaminopyridine (DMAP), dicyclohexylcarbodiimide (DCC), DS (obtained from *Leuconostoc* sp., MW > 500 000 Da), glutathione, *o*-phenylenediamine (OPD), and SU were obtained from Sigma, India. All other reagents and chemicals were of synthetic grade.

Rabbit antihuman p53 polyclonal, mouse anti-DNA damage monoclonal IgG2b, and rabbit antihuman PCNA polyclonal were purchased from Stress Marq, Canada. Horseradish peroxidase-conjugated secondary antibodies were from Santa Cruz.

Carboxyl-functionalized MWCNTs (0.6 μ mol, COOH per mg of CNT), amino-functionalized MWCNTs (1.5 μ mol, NH₂ per mg of CNT), and graphene (99.9% carbon) were obtained from United Nanotech Innovation Pvt Ltd., India. Both types of MWCNTs had an average length of 20 μ m and an average outer diameter of 20 nm as determined by high-resolution transmission electron microscopy (HRTEM). Graphene comprised 3–6 layers and measured 5–10 nm in thickness; the diameter was below 5 μ m. Amorphous carbon and total metal content, determined by thermogravimetry, was <2% w/w and <1% w/w, respectively, in MWCNTs and undetectable in grapheme.³⁸

MET was a gift from Venus Remedies, Panchkula. Mefenamic acid was a gift from Everest Formulation Pvt. Ltd., Solan, while cetirizine was a gift from Cipla, Baddi. Chlorpromazine (CPZ) was a gift from SPB Pharma Pvt. Ltd., Kumarhatti, and hydroxypropyl- β -cyclodextrin (HP β CD) was a gift from Roquette. The number of free amino groups was determined by a *p*-nitrobenzaldehyde assay.³⁸

Cells and Cell Culture. Cell lines, purchased from National Centre for Cell Sciences, Pune, India, were maintained in 90% v/v Dulbecco's modified Eagle's medium (DMEM) and 10% v/v fetal bovine serum (FBS) under standard conditions (37 °C, 95% air and 5% carbon dioxide). DMEM containing phenol red was used in all assays except when stated otherwise.

Preparation of Fluorescein-Labeled NPs. Amino-functionalized MWCNTs (200 mg) and FITC (100 mg) were stirred overnight in 10 mL of carbonate buffer (pH 9.0). F-MWCNT was separated by filtration and washed several times with water and acetone to remove the unreacted dye.³⁹ The conjugation was confirmed by the formation of fluorescent MWCNTs (488 nm excitation/530 nm emission) and attenuated total reflection (ATR)–Fourier transform infrared (ATR-FTIR) as described in a later section. Carboxy-functionalized were conjugated with DTAF (DTAF-MWCNT) following the same protocol. The yield of F-MWCNT and DTAF-MWCNT was >95%.

The reaction was monitored by hourly sampling (0.1 mL) from the carbonate buffer. The reaction mixture was centrifuged (20 000g; 20 min), and the supernatant obtained was diluted 100-fold with water. The completion of the reaction was confirmed when no significant change (<2% compared to fluorescence intensity at the start of the experiment) in fluorescence intensity was observed in three consecutive time points. The complete labeling of amino groups by FITC was further confirmed by quantification of free amino groups by a colorimetric *p*-nitrobenzaldehyde assay.³⁸ No free amino groups were detected after overnight incubation of CNTs with FITC.

Graphene was acid-refluxed for 30 min and separated by centrifugation as described previously.^{20,40} The acid-functionalized graphene was labeled with DTAF as described above. Yield > 90%.

Preparation of Drug Conjugates. Liquid-Phase Esterification. F-MWCNT was conjugated with drugs using DCC/DMAP coupling in dimethylformamide. Briefly, F-MWCNT (50 mg) and drugs (5 mg) were added in dry DMF and stirred to dissolve the drug. The reaction mixture was transferred to ice; DCC (5 mg) was added and stirred for an additional 5 min. DMAP was added in a catalytic amount (1 mg), and the reaction mixture was stirred overnight at room temperature. The reaction was carried under nitrogen. The conjugates were separated by centrifugation (10 000g; 20 min) and washed with HCl, followed by saturated NaHCO₃ solution. The conjugate was then dried at room temperature. All steps were performed in the dark. The formation of conjugates (MET-F-MWCNT) was confirmed by a reduction in fluorescence intensity and FTIR. The fluorescence intensity of conjugates was typically 3–4 orders lower than that at the start of the reaction, and fluorescence was not detectable in MET-F-MWCNT.

MET was conjugated with DTAF-MWCNT as described for F-MWCNT. Yield > 95% for all conjugates. Drug loading was 2.8 μmol MET per mg of MET-F-MWCNT and 1.3 μmol MET per mg of MET-DTAF-MWCNT.

DTAF-graphene was also esterified following the same procedure. Drug loading was 1.5 μmol MET per mg of MET-DTAF-graphene.

Aspirin, mefenamic acid, and cetirizine were conjugated to F-MWCNT as described for MET-F-MWCNT. Yield > 95%

for all conjugates. Drug loading was between 2.5 and 3.0 μmol drug per mg of the drug-F-MWCNT conjugate.

Solid-Phase Esterification. F-MWCNT (50 mg), MET (5 mg), and phosphorus pentoxide (8 mg) were mixed and heated at 60 °C for 8 h. The reaction mixture was suspended in ethyl acetate and filtered through a sintered glass filter. The reaction mass retained on the filter was washed twice with saturated NaHCO₃ solution and was washed twice with distilled water. The CNTs retained on the filter were collected and dried at room temperature. The fluorescence intensity of the conjugate was approximately 60% lower than that at the start of the reaction. Yield > 90%. Drug loading was 2.2 μmol MET per mg of MET-F-MWCNT.

Suramin and Dextran Sulfate Loading. MET-F-MWCNT (1 mg) was incubated with SU or DS (10 mg) in water (1 mL) under continuous stirring in the dark for 1 h. SU@MET-F-MWCNT or DS@MET-F-MWCNT was separated by centrifugation (20 000g; 10 min) and washed twice with distilled water (2.5 mL/washing) to remove unbound SU or DS. The supernatant obtained after centrifugation and the two washings were combined, and unbound SU was determined as described elsewhere,⁴¹ while unbound DS was determined by the colorimetric anthrone method as described elsewhere.⁴² Based on the mass balance deduced from the unbound ligand content, loading was calculated at 0.1 mg of SU and 0.2 mg of DS per mg of SU@MET-F-MWCNT and DS@MET-F-MWCNT, respectively. MET-DTAF-MWCNT was loaded with SU as described for MET-F-MWCNT. Yield > 90%.

For coloaded, various concentrations of SU and DS were mixed with 1 mg of MET-F-MWCNT in 1 mL of water for 1 h. The concentrations were selected based on the DOE strategy as implemented in response surface methodology. DS+SU@MET-F-MWCNT was separated as described above, and each of the formulations was analyzed for cytotoxicity in A549 cells and cellular uptake in RAW 264.7 cells. Cytotoxicity was determined at 50 nM MET equivalents (ca. 20 μg/mL DS+SU@MET-F-MWCNT in all formulations), while cellular uptake was determined at 20 μg/mL DS+SU@MET-F-MWCNT. The changes in cytotoxicity were normalized to those observed in MET-F-MWCNT and expressed as fold change in cytotoxicity compared to MET-F-MWCNT. Cellular uptake was expressed as a percentage of DS+SU@MET-F-MWCNT (20 μg/mL) internalized by RAW 264.7 cells.

The optimized formulation was prepared by stirring MET-F-MWCNT (1 mg), SU (10 mg), and DS (8.1 mg) in water (1 mL) for 1 h. The optimized formulation was separated by centrifugation and washed twice with distilled water (2.5 mL/washing) as described above. The supernatant obtained after centrifugation and the two washings were combined, and two aliquots (0.5 and 5 mL) were drawn to determine unbound DS and SU. The first part (0.5 mL) was subjected to the colorimetric anthrone method as described above to determine the amount of unbound DS. The second part (5 mL) was evaporated to dryness on a water bath, and the weight of the residue was determined. The amount of unbound DS, calculated by the anthrone method, was deducted from the weight of dry residue to obtain the amount of unbound SU. Based on colorimetric analysis of unbound DS and gravimetric analysis of SU, 0.08 mg of SU and 0.15 mg of DS were loaded per mg of DS+SU@MET-F-MWCNT. Yield > 90%.

DS+SU@MET-DTAF-graphene was prepared by stirring MET-F-MWCNT (1 mg), SU (10 mg), and DS (10 mg) in

water (1 mL) for 1 h. The separation and quantification of DS/SU were performed as described for DS+SU@MET-F-MWCNT. Yield > 90%.

Characterization of Drug Conjugates. An aqueous suspension of MWCNTs was placed on copper grids, air-dried, and viewed under HRTEM. An aqueous suspension of DS+SU@MET-F-MWCNT was placed on a glass coverslip and air-dried. The coverslip was sputter-coated with gold and subjected to EDX, attached to a scanning electron microscope, at 20 keV accelerating voltage. All conjugates were placed on the diamond crystal of ATR-FTIR, and the spectrum was recorded without any sample preparation steps.

Hydrolysis of Conjugates. Confluent cultures of A549 cells were trypsinized, and the cell suspension was washed three times with warm PBS (pH 7.4). The cells were then dispersed in cold PBS and lysed in a bath sonicator for 5 min. The lysate was clarified by sequential centrifugation (10 000g; 10 min) and filtration (0.45 μ m membrane filter). The protein content in the lysate was determined by the Bradford method. The homogenate was then suitably diluted with PBS to obtain 0.1 mg protein/mL.

MET-F-MWCNT, MET-DTAF-MWCNT, or SU@MET-F-MWCNT were dispersed in PBS (0.2 mg CNT/mL) immediately before use. PBS (0.1 mL), A549 cell lysate (0.1 mL), or A549 cell lysate containing 2 mM NaF (0.1 mL) were mixed with conjugates (0.1 mL) in black 96-well plates. The final concentration of conjugates was 0.1 mg/mL. Fluorescence intensity (488 nm excitation/530 nm emission) was recorded at 1 min intervals for 60 min. The rate of hydrolysis was expressed as the rate of change of fluorescence intensity per minute.⁴³

Intracellular degradation was determined in A549 cells. Approximately 10 000 cells/well/200 μ L were seeded in black 96-well plates and incubated overnight in 90% DMEM/10% FBS (v/v). The cells were once washed with sterile PBS and then replaced with 90% DMEM/10% FBS containing 0.5 mg/mL of MET-F-MWCNT, MET-DTAF-MWCNT, or SU@MET-F-MWCNT for 1 h. The cells were extensively washed with warm PBS to remove extracellular conjugates. The cells were further incubated for 6 h in a serum-free medium (DMEM without phenol red). Cells were lysed at 15 min intervals during the 6 h of incubation (3–6 wells for each conjugate) as described earlier,²⁰ and the fluorescence intensity was recorded using a microplate fluorimeter.

To determine the intracellular site of hydrolysis, cells were trypsinized after 6 h and suspended in cold lysis buffer (pH 7.4) containing 20 mM HEPES, 10 mM KCl, 2 mM MgCl₂, 1 mM EDTA, and 1 mM EGTA. Cells were repeatedly passed through a 26 gauge needle for lysis. The fluorescence intensity of the lysate was determined as described above. The lysate was then centrifuged at 1000g for 10 min to separate nuclei and cell debris. The supernatant was collected and centrifuged at 10 000g for 5 min to remove lysosomes and mitochondria. The fluorescence intensity of supernatant (cytosolic fraction) was determined. The pellet containing lysosomes and mitochondria was resuspended in lysis buffer and subjected to fluorimetry. The absence of lysosomes and mitochondria in the cytosolic fraction was confirmed by the absence of *N*-acetyl- β -D-glucosaminidase (lysosomal marker), an monoamine oxidase (mitochondrial marker) in the cytosolic fraction.⁴⁴

Correlation between Fluorescence Intensity and Drug Release. MET-F-MWCNT (10 mg) was mixed with 0.5 mL of PBS and 0.5 mL of A549 cell lysate in 1.5 mL

microcentrifuge tubes. The microcentrifuge tube was incubated at 37 °C in a shaker incubator for up to 2 h, and aliquots of 0.1 mL were drawn at regular intervals. The aliquots were diluted to 1.1 mL with the incubation medium (1:1 PBS/A549 cell lysate v/v) and centrifuged. The supernatant was collected, and drug release was determined spectrophotometrically at 297 nm using the incubation medium as a blank. The drug concentration was calculated from a standard plot prepared using pure drug dissolved in the incubation medium. The pellet obtained after centrifugation of diluted aliquots was washed twice with cold water and suspended in 1 mL water containing 0.1% v/v Tween-80. The suspension was further diluted to 10 mL with water and transferred to a black 96-well plate (0.2 mL/well) for fluorescence measurements (488 nm excitation/530 nm emission). The fluorescence intensity and drug concentration in aliquots were determined immediately after sampling.

pH-Dependent Fluorescence Emission. F-MWCNT (1 mg) was mixed with 1 mL of 20 mM HEPES/Tris buffer at different pH values (pH 6.0, 6.5, 7.0, 7.5, and 8.0). The pH range was selected to encompass the pH values observed in normal (slightly basic) and tumor tissues (near neutral to slightly acidic). After 5 min, aliquots of 0.1 mL were transferred to black 96-well plates, and fluorescence emission was determined at 530 nm following excitation at 450 and 490 nm. The ratio of emission at the two excitation wavelengths (490 nm/450 nm) was determined.⁴⁵

Preparation of CNT Suspension. For cell-based assays, the conjugates were prepared under aseptic conditions using autoclaved/filter-sterilized solutions and reagents. The sterility was confirmed by spreading or dispersing 1 mg of conjugates on solid and in liquid media, respectively. Bacterial growth was determined on nutrient agar and in Mueller–Hinton broth, while fungal growth was determined on potato dextrose agar and in YPD broth. No microbial growth was observed in any of the four media after 72 h of incubation at 37 °C. Further, the yeast media were also maintained at 25 °C for 72 h without evidence of any detectable fungal growth.

All conjugates were dispersed at 1 mg/mL in 90% DMEM/10% FBS by bath sonication for 10 min. The stock solution was appropriately diluted in a culture medium to obtain desired concentrations, and each working concentration was briefly sonicated. The stability of all working concentrations was assessed visually and by optical microscopy.³⁹ No visual signs of aggregation or settling were observed up to a concentration of 0.5 mg/mL in all conjugates except F-MWCNT; the latter suspension was stable up to 0.1 mg/mL.

DS and SU Desorption. Amino-functionalized MWCNTs and DS were labeled with RBITC (RBITC-MWCNT) and DTAF (DS-DTAF), respectively, as described earlier.³⁹ DS+SU@MET-F-MWCNT, DS-DTAF+SU@MET-F-MWCNT, or DS-DTAF+SU@RBITC-MWCNT were prepared using DS or DS-DTAF as described above. DS+SU@MET-F-MWCNT was incubated in A549 cell extracts as described for hydrolysis studies. MWCNTs were extracted by centrifugation after 6 h (10 000g; 20 min). The pellet was extracted several times with methanol, dried under nitrogen, and dissolved in water. The fluorescence was recorded at excitation and emission wavelengths at 315 and 405 nm, respectively.⁴⁶ Additionally, fluorescence was also determined at 360 nm excitation and 400 nm emission.⁴⁷ The SU concentration was also determined in the supernatant at 315/405 nm and 360/400 nm excitation/emission pairs. Similarly, DS-DTAF+SU@MET-F-MWCNT

were recovered by centrifugation after 6 h of incubation in A549 cell extracts. The pellet was redispersed in water, and fluorescence was determined at excitation and emission wavelengths 488 and 530 nm, respectively. The sorption of DS on MWCNT was further confirmed by the fluorescence resonance energy transfer (FRET) as described in a previous report.³⁹ Briefly, DS-DTAF+SU@RBITC-MWCNT were recovered by centrifugation after 6 h of incubation in A549 cell extracts, and the pellet was observed under a confocal microscope using excitation and emission pairs specific for the donor (fluorescein) and acceptor (rhodamine). The difference in fluorescence intensity of the acceptor after excitation with a wavelength specific for acceptor and donor was used to determine FRET efficiency.

In all analyses, blank samples were run (water alone or A549 cell lysate alone), and blank measurements were subtracted from standard and sample measurements. The concentration of SU and DS-DTAF was determined from standard plots prepared using SU or DS-DTAF in water or A549 cell lysates. Desorption of DS-DTAF and SU was determined in phenol red-free DMEM supplemented with 10% FBS or water by fluorimetry as described above. The mass balance (sorbed on MWCNT + desorbed and released in cell lysate/culture medium/water) was >90% in all cases.

DS (10 mg/mL in water; 200 μ L) was added in high-binding, flat-bottom 96-well plates and incubated for 3 h. DS solution was gently aspirated, and the wells were washed with water several times until DS was not detected in washings by the anthrone method. Based on mass balance, DS coating was ca. 177 ± 28 μ g/well. The SU solution (100 μ g/mL in water; 200 μ L) was added to the wells and incubated for 1 h. The solution was gently aspirated, and the SU concentration was determined fluorimetrically. The recovered SU solution did not show a positive reaction by the anthrone method, indicating DS is not desorbed during the course of incubation with SU.

Cellular Uptake Assay. A549, RAW 264.7, MCF-7, HepG2, Hep3B, PC-12, MOLT-4, NCI-H30, and PLC/PRF/5 cells (10 000 cells/well/200 μ L in 96-well plate) were incubated with 100 μ g/mL of F-MWCNT and MET-F-MWCNT for 6 h at 37 °C in DMEM containing 10% FCS (pH 7.2). A549 cells were also incubated with MET-F-MWCNT for 6 h at 4 °C or at 37 °C in the presence of 100 μ M folic acid or 100 μ M MET in a routine culture medium (DMEM containing 10% FCS pH 7.2) or culture medium acidified with HCl to achieve pH 6.5. A549 and RAW 264.7 cells were also incubated with 100 μ g/mL DS@MET-F-MWCNT for 6 h at 37 °C in DMEM containing 10% FCS (pH 7.2). After incubation, the cells were washed up to 5 times with warm PBS to remove extracellular CNTs, and cells were lysed with 0.1% v/v Tween-80. Cell uptake was determined by estimating the CNT concentration in cell lysates spectrophotometrically, as described earlier.²⁰ Cell uptake was expressed as the % of total CNT (100 μ g/mL) present in cell lysates.

A549 cells were incubated with 100 μ g/mL DS+SU@MET-F-MWCNT either at 4 °C or in the presence of 3 mg/mL sodium azide, 10 μ g/mL CPZ, or 10 mM HP β CD. Cell uptake was quantified spectrophotometrically after 6 h.^{20,48,49} A549 cells incubated with 100 μ g/mL DS+SU@MET-F-MWCNT for 6 h were fixed in 2.5% paraformaldehyde (prepared in PBS) for 15 min and washed. The nuclei were stained with 25 μ g/mL propidium iodide for 30 min and then observed under a confocal microscope.

Biocompatibility and Cytotoxicity Assays. Biocompatibility of F-MWCNT was determined by methods described earlier³⁹ unless specified otherwise. MWCNTs were found to quench fluorescence even at low concentrations (>10 μ g/mL); therefore, wherever feasible, spectrophotometric methods were employed and adjusted for interference by MWCNTs as described earlier.^{39,50}

Cell viability was determined in A549 cells by an MTT assay. Briefly, approximately 10 000 cells/well/200 μ L were seeded in 96-well plates and incubated with different concentrations of F-MWCNT (0.01–100 μ g/mL), free MET (0.01–1000 nM), and drug conjugates (equivalent to 0.1–1000 nM MET) for 72 h. A stock solution of MTT (5 mg/mL) was added to each well (20 μ L/well) and incubated for 3 h. Formazon was then dissolved in 100 μ L of 20% w/v sodium dodecyl sulfate (prepared in 0.01 M hydrochloric acid), and the absorbance was recorded at 595 nm. Cell viability was determined by considering the absorbance of the control as 100% viability.³⁹

A549 cells were incubated with 10 μ g/mL of MWCNTs (and free MET, wherever applicable) for 72 h as described above, except lysosomal and mitochondrial integrity assays, where cells were incubated for 24 h. Lysosomal and mitochondrial integrity was determined by neutral red uptake and safranin O uptake assays.³⁹ Induction of oxidative stress was determined by a spectrophotometric assay of protein carbonylation as described elsewhere⁵¹ and the formation of oxidative DNA products (8-hydroxydeoxyguanosine [8-OHdG]) by whole-cell ELISA as described below. DNA damage was further confirmed by a diphenylamine assay,³⁹ and induction of DNA damage response and consequent cell cycle arrest were determined by p53 and PCNA assays, respectively.

8-OHdG, p53, and PCNA expression was determined by whole-cell ELISA as described elsewhere.⁵² Briefly, A549 cells were treated with free MET or drug conjugates for 72 h. The culture medium was removed, and cells were washed twice with 0.01 M PBS (pH 7.2) to remove extracellular CNTs and debris. The cells were then fixed in 2% w/v paraformaldehyde (prepared in PBS) at 4 °C for 30 min. The fixed cells were then incubated in solution A (0.05% v/v Tween-20 dissolved in PBS) for 2 min. The solution was replaced with solution B (1% w/v BSA dissolved in PBS) for 2 h, followed by primary antibodies (1:200 for anti-p53 and anti-PCNA; 1:500 for anti-8-OHdG) for 1 h. The primary antibodies were diluted to the desired concentration in solution C (PBS containing 0.05% v/v Tween-20 and 1% w/v BSA). The primary antibodies were removed and cells washed 5 times with solution A. The secondary antibody was diluted 1:300 in solution C and incubated with cells for 2 h. The cells were extensively washed with solution A, followed by the OPD solution. Following color development, the reaction was quenched with acid and absorbance determined at 492 nm. The acid-quenched OPD solution was then replaced with methylene blue solution to determine cell number.⁵² OPD absorbance was then normalized to cell number.

The cell migration assay was performed as described elsewhere with minor modifications.⁵³ Briefly, A549 cells were suspended in serum-free RPMI-1640 (5×10^5 cells/mL) and placed in the upper chamber (600 μ L). RPMI-1640 supplemented with 10% FBS was placed in the lower chamber (600 μ L). MET (1 μ M) or an equivalent amount of MET-F-MWCNT, DS @MET-F-MWCNT, SU@MET-F-MWCNT, and DS+SU@MET-F-MWCNT were added in the upper

chamber. CNT conjugates were dispersed in serum-free RPMI-1640 by bath sonication to obtain a 100 $\mu\text{g}/\text{mL}$ suspension. The suspensions were adequately diluted with serum-free RPMI-1640 to obtain the desired concentration in the upper chamber. Two sets of control were included: CNT-free control and CNT control. The CNT-free control set contained serum-free RPMI-1640 in the upper chamber, while the CNT control contained 50 $\mu\text{g}/\text{mL}$ F-MWCNT in the upper chamber. Following incubation for 24 h, the cells that migrated to the lower side of the upper chamber were fixed with cold methanol, stained with crystal violet (0.5% w/v; 30 min), and gently washed in water to remove excess dye. The dye was extracted with 1 mL of 10% acetic acid and was determined at 595 nm. The absorbance of control wells was considered 100%, and absorbance in MET/conjugate-treated groups was expressed as % absorbance relative to the control. The cell invasion assay was performed as above except that collagen-coated transwell inserts were employed.⁵⁴

Computational Analysis. The structure of MET-F-MWCNT was generated in ChemBioDraw, and energy was minimized in ChemBio3D using an MMF force field. The energy minimized structure was saved in mol2 format. The CNT was modeled as a single layer of (10,10) CNT in an armchair configuration, and a single MET molecule was attached to the hydroxyl group of fluorescein. These two simplifications in the structure of MET-F-MWCNT were adopted to reduce computational time and artifacts arising due to nonspecific binding of a more elaborate structure (multi-layered CNT and two MET per fluorescein). MET-F-linker was generated by deleting the CNT structure from MET-F-MWCNT, and the energy-minimized structure was saved in mol2 format. The crystal structures of FR α (FR1), FR β (FR2), and DHFR were obtained from the Protein Data Bank (PDB entries 5IZQ, 4KN0, and 1U72, respectively). The crystal structures of RFC and PCFT are not available; hence, their protein sequences were obtained from UniProt (UniProt IDs P41440 and Q96NT5, respectively). The homology model was constructed using a bacterial glycerol-3-phosphate transporter (PDB entry 1PW4) as a template as described elsewhere^{55,56} on the SWISS-MODEL server (<https://swissmodel.expasy.org/>).⁴⁴ The ligands (MET-F-MWCNT and MET-F-linker) and proteins were prepared for docking using the AutoDock-Tools module in MGLTools. The docking of ligands was performed in FR α , FR β , DHFR, RFC, and PCFT using AutoDock Vina⁵⁷ available on the Opal2 server (<http://nbc-222.ucsd.edu/>),^{45,58} and output files were analyzed using PyMol.

The ligand-based screening was performed using MET conformation in the DHFR crystal structure (PDB entry 1U72) as a template. Conformations of MET-F-MWCNT and MET-F-linker were generated using Balloon^{50,59} and compared with the template MET conformation using ShaEP.⁶⁰

The protein-mediated, nontarget interaction of F-MWCNT, MET-F-MWCNT, and MET-F-linker was determined using PharmMapper.^{55,56,61} The mol2 files of F-MWCNT, MET-F-MWCNT, and MET-F-linker were submitted to PharmMapper server (<http://www.lilab-ecust.cn/pharmmapper/submitjob.html>). The default options of the server were selected, which comprised the generation of 300 conformers for comparison with pharmacophores and an output of 300 best-matched targets. The possible interactions of F-MWCNT, MET-F-MWCNT, and MET-F-linker with biomolecules were also determined using the Ultrafast Shape Recognition-Virtual

Screening (USR-VS) server (<http://usr.marseille.inserm.fr/>).⁶² This server compares the conformations of the query compound against a database of 93.9 million 3D conformers obtained from 23.1 million molecules. The server enables querying the input structures using two flavors of the database, the original USR, which compares the shape of the input structure with a database of conformers.⁶³ USRCAT is an extension of USR, which incorporates pharmacophoric information during the comparison process.⁶⁴

MD Simulations. All input files were generated using CHARMM-GUI (<http://www.charmm-gui.org/>).⁶⁵

DHFR was obtained from PDB (1U72) and MET, and water was removed using PDB Reader.⁶⁶ The structure containing DHFR, along with cofactor NADPH, was prepared using PDB Reader. The best pose conformation of the MET-F-linker binding to DHFR (obtained from docking studies) was prepared using the Ligand Reader and Modeler.⁶⁷ DHFR, with bound NADPH, was combined with MET-F-linker using VMD⁶⁸ and solvated, and neutralizing ions were added. The solvated box was equilibrated with the NVT ensemble for 125 000 steps (2 fs/step) using Langevin piston followed by a production run for 50 ns using the NPT ensemble. The temperature was kept at 310.15 K. Simulations were performed using the NAMD and CHARMM force field.^{69–71}

A (6,6) CNT was generated using the Nanomaterial Modeler available on CHARMM-GUI. The CNT generated was 36.9 Å long and 8.1 Å in diameter. A single layer of CNT was generated to reduce the computational cost required to run the simulations.

DS is a linear polysaccharide composed primarily of α -1,6-linked D-glucose (ca. 95%) with occasional branching occurring as 1,2-, 1,3-, and 1,4-linkages. The glucose residues are mainly disulfated: 2,3-disulfonation is most common, while 3,4- and 2,4-disulfonation occur relatively at lower proportions.^{72,73} DS was modeled using Glycan Reader and Modeler.^{74–76} DS was modeled as a linear decamer of α -1,6-linked D-glucose^{72,73} with 2,3-disulfonation at all residues except 2,4-disulfonation at residue 3 and 3,4-disulfonation at residue 6.

SU was modeled using the Ligand Reader and Modeler.⁶⁷ The structure of suramin was obtained from PDB (PDB ligand ID SVR), and the acid form was converted to the hexaanion form by removing hydrogen atoms from the six sulfate groups.

The input files generated above were combined using Multicomponent Assembler available on CHARMM-GUI. Two systems were generated, with one comprising CNT and a molecule of DS, while the other comprised CNT and a molecule of SU. The simulation was run in a box of $50 \times 50 \times 50 \text{ \AA}^3$. The box was solvated with TIP3P water⁴⁹ and charge neutralized with an appropriate number of sodium ions (6 Na⁺ for SU and 20 Na⁺ for DS). The solvated box was equilibrated with the NVT ensemble for 125 000 steps (2 fs/step) using Langevin piston followed by a production run for 50 ns using the NPT ensemble. The temperature was kept at 310.15 K. Simulations were performed using the NAMD and CHARMM force field.^{69–71} Another system contained one molecule each of DS and SU, 26 sodium ions, and water molecules. The equilibration and simulations were performed; for systems containing CNT, that simulation was run for 150 ns. The longer simulation was required in the latter system because the convergence of the system was observed after 50 ns. The data was postprocessed using CPPTRAJ⁷⁷ and VMD.⁶⁸

Statistical Analysis. Data was converted to the mean and standard deviation (SD) and expressed as the mean \pm SD. The data for two groups were compared by *t*-test, while a multiple group comparison was performed by one-way analysis of variance followed by *post hoc* Tukey's test using SigmPlot. The differences were considered significant at $p < 0.05$. Comparison between predicted and measured drug concentrations by Bland–Altman, Passing–Bablok, Deming, and Mountain plots was performed using MedCalc.

In the case of parameters expressed as fold change compared to the control (protein carbonylation, DNA damage, p53, and PCNA level), the parameter was determined separately for the control and treatment groups and converted to mean \pm SD. The mean fold change was calculated as ratios of mean values in the treatment and control groups. The SD of ratios was calculated using Taylor's second-moment expansion:

$$SD = R \sqrt{\left(\frac{SD_T}{\text{mean}_T}\right)^2 + \left(\frac{SD_C}{\text{mean}_C}\right)^2}$$

where SD_T and SD_C represent the SD of treatment and control groups, respectively, mean_T and mean_C represent the mean of treatment and control groups, respectively, and R represents the ratio of mean_T and mean_C .

The fold difference in the cellular uptake of F-MWCNT and MET-F-MWCNT in each cell line was determined in a similar way. Briefly, cellular uptake of F-MWCNT and MET-F-MWCNT was converted to the mean \pm SD for each cell line. The mean fold difference (R) was calculated as ratios of mean cellular uptake of MET-F-MWCNT and F-MWCNT. The SD of ratios was calculated using the following formula:

$$SD = R \sqrt{\left(\frac{SD_M}{\text{mean}_M}\right)^2 + \left(\frac{SD_F}{\text{mean}_F}\right)^2}$$

where SD_M and SD_F represent SD of MET-F-MWCNT and F-MWCNT groups, respectively, mean_M and mean_F represent mean cellular uptake of MET-F-MWCNT and F-MWCNT in a cell line, respectively, and R represents the ratio of mean_M and mean_F .

The fold change in cytotoxicity between DS+SU@MET-F-MWCNT compared to MET-F-MWCNT in A549 cells was determined in a similar manner.

RESULTS AND DISCUSSION

Synthesis of Drug-MWCNT Conjugate and Real-Time Release Monitoring of Drug Release. The development of the platform was based on the principle that fluorescence of fluorescein is quenched following esterification of its phenolic groups; the fluorescence is recovered following hydrolysis of the ester group.⁴³ The schematic representation of the principle is shown in Figure 1. Fluorescein-labeled multiwalled CNTs (F-MWCNTs) were prepared by reaction of amino-functionalized MWCNTs with FITC. F-MWCNTs were conjugated with MET using a liquid-phase and a solid-phase esterification protocol to obtain MET-F-MWCNT. The liquid-phase esterification was performed by DMAP/DCC coupling in dimethylformamide, while solid-phase esterification was performed using phosphorus pentoxide. The reaction proceeded to completion in the liquid-phase method, as evident from the complete loss of fluorescence in the esterification product (MET-F-MWCNT). On the other

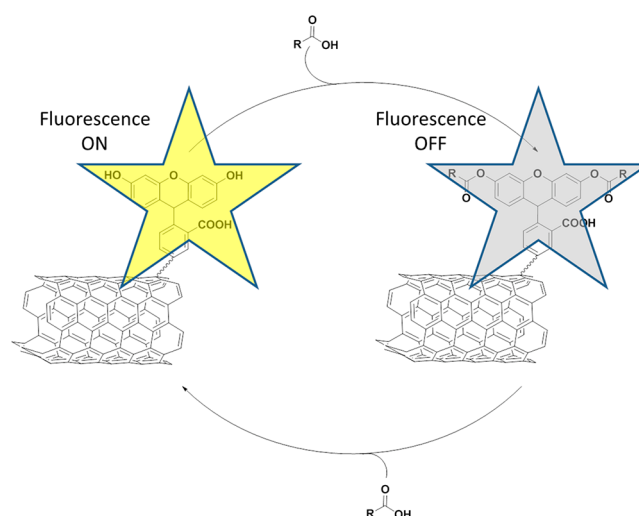


Figure 1. Schematic representation of the fluorescence turn-on platform for real-time monitoring of drug release.

hand, the solid-phase protocol was much less efficient (ca. 60%) and hence not investigated further. MET-F-MWCNT was therefore synthesized using DMAP/DCC coupling in dimethylformamide. The formation of MET-F-MWCNT was confirmed by Fourier transform infrared spectroscopy (Figure S1). As shown in Figure 2, the HRTEM of MET-F-MWCNT revealed that the structural integrity of MWCNTs was not compromised following the formation of conjugates.

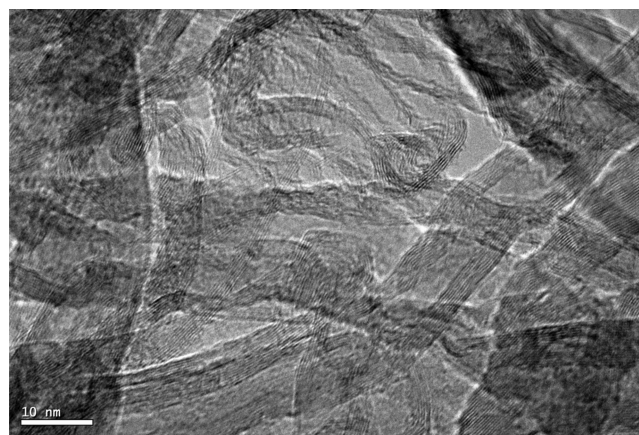


Figure 2. HRTEM of MET-F-MWCNT.

To validate the feasibility of employing the fluorescence turn-on system, hydrolysis of MET-F-MWCNT was monitored in phosphate-buffered saline (PBS) and A549 cell lysate. The rate of hydrolysis of the conjugate was negligible in the presence of PBS, while a significantly higher rate of hydrolysis was observed in the presence of A549 cell lysate (Figure 3A, Table 1), suggesting that drug release is faster in intracellular compartments and that the intracellular drug release rate is faster than spontaneous hydrolysis observed in PBS. As observed in Figure 3A, no fluorescence was observed at the start of the experiment (0 min). This is because covalent modification of $-OH$ groups of fluorescein with drug molecule resulted in fluorescence quenching.^{43,78} With an increase in incubation time, the intensity of green fluorescence started increasing, suggesting that the drug molecules have cleaved

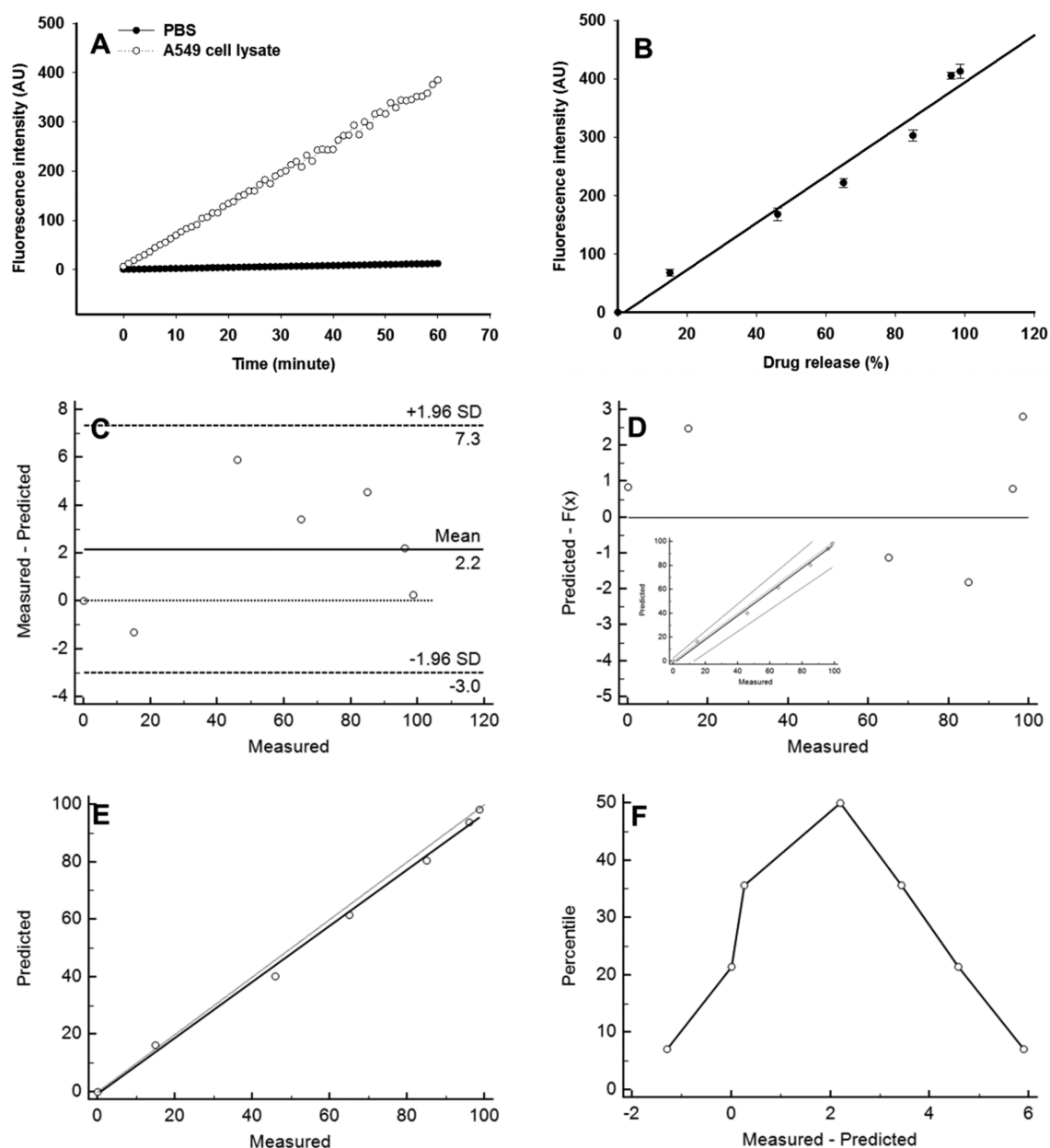


Figure 3. (A) A representative hydrolysis profile of MET-F-MWCNT in phosphate-buffered saline (PBS; pH 7.4) and A549 cell lysate. (B) Correlation between drug release and fluorescence intensity in the presence of A549 cell lysate. (C–F) Correlation between measured drug release and drug release predicted from fluorescence measurements in panel B. Panels D and E represent Bland–Altman and Passing–Bablok residual plots, respectively. The inset in panel D represents the Passing–Bablok regression; the solid black line shows the regression line, the solid gray line represents the line of equality (slope = 1), and dotted lines show 95% confidence intervals. Panels E and F represent the Deming regression line and mountain plot, respectively. MET-F-MWCNT were incubated in PBS or A549 cell lysate, and fluorescence intensity was determined at regular intervals as described in the [Materials and Methods](#) section. Drug release was determined spectrophotometrically. The rate of hydrolysis is expressed as an increase in fluorescence intensity (arbitrary units) per minute. Data is the mean \pm SD of triplicate samples per data point in panel B.

from the $-OH$ groups of fluorescein, resulting in the recovery of fluorescence. Quantitative analysis revealed that the rate of hydrolysis was over 30 times higher in A549 cell lysate compared to the rate in PBS. Further, a linear correlation ($R^2 > 0.9$) between drug release and fluorescence intensity was also observed (Figure 3B). The ability to predict drug release from fluorescence measurements was further verified using residual plots and regression analysis. Bland–Altman residual plots revealed an average 2.2% underestimation of drug release

calculated/predicted from fluorescence measurements compared to measured concentrations (Figure 3C). Similarly, the Passing–Bablok residual plot and regression analysis (Figure 3D) as well as Deming regression (Figure 3E) revealed a good agreement between predicted and measured drug concentrations. The cusum test for linearity indicated no significant deviation from linearity ($p = 0.43$) in the Passing–Bablok plot, while the Deming regression revealed a slope of 0.9774. Mountain plot revealed an underestimation of about 2% in the

Table 1. Hydrolysis of Conjugates in Phosphate-Buffered Saline (PBS; pH 7.4), A549 Cell Lysate, and A549 Cells^a

conjugate	rate of hydrolysis ($\Delta F/\text{min}$)		
	PBS	A549 cell lysate	A549 cells
MET-F-MWCNT	0.2 \pm 0.0	6.0 \pm 0.6 ^c	1.1 \pm 0.1 ^b
SU@MET-F-MWCNT	0.2 \pm 0.0	5.1 \pm 0.6 ^c	1.2 \pm 0.1 ^b
MET-DTAF-MWCNT	0.2 \pm 0.0	6.5 \pm 0.5 ^c	1.1 \pm 0.1 ^b

^aMET-F-MWCNT were incubated in PBS, A549 cell lysate, or A549 cells, and fluorescence intensity was determined at regular intervals as described in the **Materials and methods** section. The rate of hydrolysis is expressed as an increase in fluorescence intensity (arbitrary units) per minute. Data is the mean \pm SD of 3–6 samples per treatment group. ^b $p < 0.05$ with respect to hydrolysis in PBS by one-way ANOVA followed by *post hoc* Tukey's test. ^c $p < 0.001$ with respect to hydrolysis in PBS by one-way ANOVA followed by *post hoc* Tukey's test.

50th percentile and an underestimation of more than 5% in the 17th percentile (Figure 3F). These results suggest a good agreement between the measured drug concentrations and the concentrations predicted from fluorescence measurements.

Intracellular hydrolysis in A549 cells appears to occur at a much lower rate compared to A549 cell lysate (Table 1). This is not surprising given the fact that only a fraction of MET-F-MWCNT could enter the cells and are accessible for action by the intracellular hydrolytic enzymes. On the other hand, the entire bulk of MET-F-MWCNT is accessible to esterases in cell lysates resulting in a higher rate of hydrolysis.

The intracellular hydrolysis of CNTs is expected to be mediated by the action of nonspecific esterases. To verify the involvement of esterases in accelerated drug release under intracellular conditions, MET-F-MWCNT was incubated with A549 cell lysate in the presence of an esterase inhibitor (sodium fluoride; 1 mM final concentration).^{79,80} The drug release was significantly reduced in the presence of NaF and was similar to that observed in PBS suggesting that only spontaneous hydrolysis contributes to drug release in the presence of NaF (0.3 \pm 0.1 $\Delta F/\text{min}$). However, NaF did not affect drug release in CNTs incubated with PBS alone, suggesting that NaF reduces drug release by acting on cellular components (0.2 \pm 0.1 $\Delta F/\text{min}$). Fractionation of cellular components revealed that cytoplasm was the site of hydrolysis since 85 \pm 6% of total cellular fluorescence was present in the cytoplasmic fraction while <10% of total cellular fluorescence was detected in the organelle fraction. This small fraction of fluorescence could be attributed to entrapment of F-MWCNT in the pellet rather than actual trafficking in these organelles. The cytoplasmic trafficking of F-MWCNTs was further confirmed by microscopy (data not shown).

Fluorescein and its derivatives, either free or conjugated to macromolecules, are known to exhibit pH-dependent changes in fluorescence spectral properties. This property has often been employed to determine cytoplasmic and organelle pH using fluorescein derivatives and fluorescein-conjugated dextrans. This is based on the principle that the emission intensity of fluorescein at 530 nm is proportional to the pH of the medium following excitation at 450 nm but pH-independent following excitation at 490 nm. Hence, the ratio of emission intensities at 530 nm following excitation at both the wavelengths (490 nm/450 nm) provides an estimate of the pH.⁴⁵ The 490/450 nm ratios at pH 6.0, 6.5, 7.0, 7.5, and 8.0 were 2.4 \pm 0.1, 4.0 \pm 0.1, 4.4 \pm 0.4, 4.9 \pm 0.1, and 5.0 \pm 0.2,

respectively (mean \pm SD of triplicate samples). It is an established fact that the extracellular pH in tumor tissues is slightly acidic compared to a slightly basic extracellular pH of the corresponding normal tissues, with a pH difference of 0.3–0.7 units. In contrast, the intracellular pH of tumor cells is similar or slightly more basic compared to corresponding normal tissues.⁸¹ F-MWCNT could, thus, not only reveal the spatial and temporal nature of drug release due to fluorescence turn-on mechanism but also provide information on the milieu at the site of drug release due to its “pH-reporter” properties. The 490/450 nm ratios could thus be exploited to determine the site of drug release in tumor tissues (acidic extracellular versus slightly basic intracellular).

Cytotoxicity of Drug Conjugate and Modulation by Suramin. CNT-based platforms have been reported to be cytotoxic and enhance the activity of anticancer drugs.^{38,82} Therefore, *in vitro* cytotoxic activity of F-MWCNT and MET-F-MWCNT was determined in a human lung cancer cell line (A549). The IC₅₀ values of MET-F-MWCNT (equivalent to the amount of MET loaded on MET-F-MWCNT) were found to be almost half of that observed with free MET (Table 2; Figure 4A). The IC₅₀ of F-MWCNT was >100 $\mu\text{g}/\text{mL}$ (Figure 4B), suggesting the biocompatible nature of the theranostic platform.

Table 2. Cytotoxicity of Conjugates in Cell Lines^a

conjugate	IC ₅₀ (nM)		
	A549	MCF-7	MOLT-4
free MET	35.6 \pm 5.8	123.5 \pm 11.0	14.6 \pm 2.3
MET-F-MWCNT (2.8) ^b	15.8 \pm 2.6 ^d	56.9 \pm 6.5 ^d	6.6 \pm 1.0 ^d
SU@MET-F-MWCNT (2.5) ^b	6.8 \pm 1.4 ^d	36.6 \pm 4.6 ^d	3.3 \pm 0.5 ^d
MET-DTAF-MWCNT (1.3) ^b	18.6 \pm 3.3 ^d		
SU@MET-DTAF-MWCNT (1.2) ^b	7.7 \pm 2.4 ^d		

^aCells were incubated with free MET or drug conjugates for 72 h, and cell viability was determined by an MTT assay. The IC₅₀ of drug conjugates is expressed in terms of the amount of conjugated MET added to cells. Data is the mean \pm SD of 2 experiments ($n = 3$ per concentration/treatment group). ^bValues in parentheses indicate the amount of MET (in μmol) per mg of the conjugate. ^d $p < 0.001$ with respect to free MET by one-way ANOVA followed by *post hoc* Tukey's test.

Further, F-MWCNT showed a decrease in mitochondrial integrity (86.6 \pm 5.8%) compared to the control (100.0 \pm 6.8%; $p < 0.05$ by *t*-test). This was accompanied by a statistically significant increase in protein carbonylation (1.4 \pm 0.1-fold) compared to the control (1.0 \pm 0.1-fold; $p < 0.05$ by *t*-test). A concomitant increase in oxidative DNA damage compared to the control (1.2 \pm 0.1 vs 1.0 \pm 0.1-fold; $p < 0.05$ by *t*-test) was also observed, suggesting induction of free radical production. DNA damage was further confirmed by the diphenylamine assay (Table 3). p53, commonly referred to as “guardian of the genome”, is an important transcription factor activated in response to DNA damage and is a key regulator of apoptosis and cell cycle arrest. p53 levels were found to be elevated in F-MWCNT-treated cells, suggesting activation of DNA damage response. Proliferating cell nuclear antigen (PCNA) is an important marker of cell cycle and is decreased in cells undergoing cell cycle arrest. A decrease in expression of PCNA following incubation with FITC-MWCNT suggested

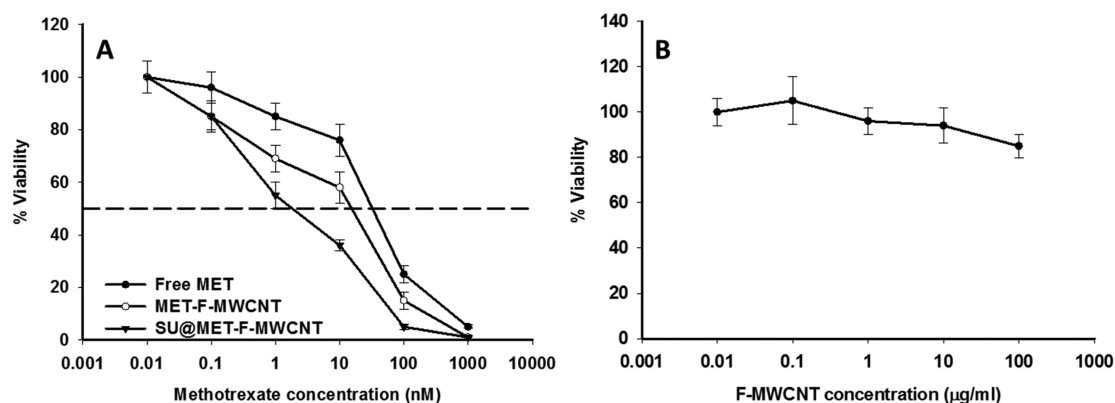


Figure 4. Cytotoxicity of free MET and drug conjugates (A) and F-MWCNT (B) in A549 cells. Cells were incubated with free MET, drug conjugates, or F-MWCNT for 72 h, and cell viability was determined by an MTT assay. The dashed line in panel A represents 50% cell viability. Data is the mean \pm SD of 2 experiments ($n = 3$ per concentration/treatment group).

Table 3. Effect on Cellular and Molecular Parameters in A549 Cells^a

treatment	DNA damage	p53 level	PCNA level
control	1.0 \pm 0.1	1.0 \pm 0.1	1.0 \pm 0.1
F-MWCNT	1.3 \pm 0.1 ^b	1.2 \pm 0.1	0.8 \pm 0.2
MET-F-MWCNT	1.8 \pm 0.1 ^d	1.5 \pm 0.1 ^c	0.7 \pm 0.1
SU@MET-F-MWCNT	2.1 \pm 0.2 ^d	1.8 \pm 0.3 ^b	0.6 \pm 0.2 ^c
free MET	1.1 \pm 0.1	1.1 \pm 0.1	0.9 \pm 0.1

^aCells were incubated with free MET, drug conjugates, or F-MWCNT for 72 h. DNA damage was determined by the diphenylamine assay and p53/PCNA levels by whole-cell ELISA. Data is the mean \pm SD of 3–5 samples per treatment group. The values represent fold change compared to the control. ^b $p < 0.05$ compared to the control by one-way ANOVA followed by *post hoc* Tukey's test. ^c $p < 0.01$ compared to the control by one-way ANOVA followed by *post hoc* Tukey's test. ^d $p < 0.001$ compared to the control by one-way ANOVA followed by *post hoc* Tukey's test.

induction of the cell cycle, probably due to activation of DNA damage response via p53 upregulation. Interestingly, free MET did not significantly increase DNA damage or p53 expression, and only slightly decreased PCNA levels, while a significant increase in DNA damage and p53 expression with a concomitant decrease in PCNA levels was observed (Table 3). A plausible explanation for these observations is that MET is a folate antimetabolite and inhibits DNA synthesis. When tethered to MWCNTs, intracellular MET concentrations are expected to be higher than those achieved with free MET. MWCNTs could damage DNA by oxidative and nonoxidative mechanisms resulting in activation of a DNA damage response, leading to p53 activation. In the presence of MET, the DNA damage may be further enhanced along with decreased efficiency of DNA repair due to antimetabolite characteristics of the drug. This is clearly evident in Table 3, whereby DNA damage is the highest in MET-F-MWCNT compared to F-MWCNT or MET alone. MET alone could increase p53 expression,^{52,83} resulting in decreased expression and activity of PCNA.^{84,85} Therefore, MWCNT and MET could synergistically enhance p53 expression and induce cell cycle arrest via a decrease in PCNA expression. MET-F-MWCNT with a supramolecular assembly of SU (SU@MET-F-MWCNT) exhibited an even lower IC₅₀ compared to MET-F-MWCNT. This was accompanied by higher p53 expression and DNA damage with a concomitant decrease in PCNA expression, suggesting SU loading further enhanced antiproliferative

activity of MET. A similar trend of cytotoxicity of MWCNT conjugates was also observed in human breast cancer (MCF-7) and leukemia (MOLT-4) cells (Table 2).

CNTs are often decorated with several different types of functional groups, while the fluorescence turn-on platform reported in the present study utilizes only amino-functionalized CNTs, apparently limiting the applicability of the platform to only those CNTs harboring a free amino group. In order to demonstrate the wide applicability of the platform, carboxy-functionalized CNTs were conjugated with another fluorescein derivative, DTAF. DTAF-labeled MWCNT (DTAF-MWCNT) and FITC-labeled MWCNTs (F-MWCNT) only differed in the composition of the linker group between MWCNT and fluorescein. It is expected that both linkers (thiourea and dichlorotriazinyl) would not significantly contribute to biological activity for two reasons: first, the linker is not hydrolyzed in the biological environment, and second, the length of the linker is too small and potentially has no role in cell–CNT interactions. To prove this assertion, MET was esterified with DTAF-MWCNTs by DMAP/DCC coupling to yield MET-DTAF-MWCNT; the ATR-FTIR spectrum of MET-DTAF-MWCNT was similar to the spectrum of MET-F-MWCNT (spectrum not shown). MET-DTAF-MWCNT and MET-F-MWCNT exhibited comparable rates of hydrolysis in PBS ($p > 0.05$) and in A549 cell lysate ($p > 0.05$) as well as cytotoxicity ($p > 0.05$; Table 1). Similarly, cytotoxicity of SU@MET-DTAF-MWCNT and SU@MET-F-MWCNT was also comparable ($p > 0.05$; Table 2).

The increase in cytotoxicity of CNT-conjugated drugs is generally attributed to a Trojan horse, whereby intracellular delivery of drugs is increased due to CNT uptake. MET is internalized by a reduced folate carrier (RFC) at a physiological pH and by folate receptors (FR) and a proton-coupled folate transporter (PCFT) at an acidic pH.^{58,61} Since extracellular pH values in tumors range from slightly basic to slightly acidic,⁸¹ it may be anticipated that MET could potentially increase the cellular uptake of MWCNTs and synergistically enhance cytotoxic activity. Quantitative analysis of cellular uptake revealed that F-MWCNT and MET-F-MWCNT were internalized to the same extent by A549 cells. The cellular uptake of F-MWCNT and MET-F-MWCNT was inhibited at 4 °C, suggesting the involvement of an active carrier process, but neither folic acid nor MET inhibited cellular uptake at pH 7.2, suggesting FRs and RFC, respectively, are not involved in cellular uptake (Figure 5A).

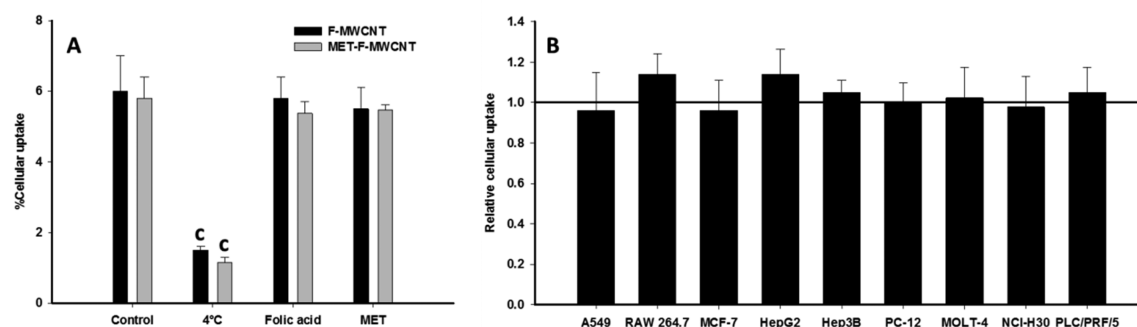


Figure 5. (A) Quantitative cellular uptake of F-MWCNT and MET-F-MWCNT in the presence of 100 μ M MET and 100 μ M folic acid and at 4 $^{\circ}$ C (pH 7.2). (B) Relative cellular uptake in cell lines expressed as the ratio of cellular uptake of MET-F-MWCNT and F-MWCNT. A549 cells were incubated with 100 μ g/mL F-MWCNT and MET-F-MWCNT for 6 h, and cellular uptake was determined spectrophotometrically. Data is the mean \pm SD of 3–5 samples per treatment group. $^{\circ}$ $p < 0.001$ compared to the control by one-way ANOVA followed by *post hoc* Tukey's test.

Further, cellular uptake at pH 6.5 was also not inhibited by folic or MET, indicating an FR- and PCFT-independent mechanism of cellular uptake (data not shown). In order to verify these findings, docking studies were performed using folate receptor α (FR α) and β (FR β), RFC, and PCFT. MET-F-MWCNT did not efficiently dock into any of these proteins, suggesting that these receptors/carriers are not involved, as evident from the comparison of the docked conformation of MET in FR β or suggested interactions of MET in FR α , RFC, and PCFT. In several docking poses, the structure of CNT was found to interact nonspecifically with nonpolar amino acid residues in the receptors/carriers, which are consistent with previous studies suggesting a π - π stacking mechanism of CNT–protein interactions. It appears plausible here that interactions of MET at the active site of receptors/carriers may be masked due to software bias toward the more prominent amino acid–CNT interactions. This software bias seems logical given the fact that only one site in MET-F-MWCNT could interact with the active site (MET), while the bulky CNT structure contains scores of potential amino acid-interacting sites (aromatic rings). Therefore, to rule out this potential bias, docking was performed by removing the CNT structure from MET-F-MWCNT (referred to as MET-F-linker). As observed with MET-F-MWCNT, MET-F-linker also exhibited inefficient docking at the target sites (Figure 6A–D). These observations suggested that the structure of MET-F-linker was probably unable to attain the requisite conformation required to bind target proteins. This assertion is complemented by experimental findings that the uptake of MET-F-MWCNT was similar to F-MWCNT, and the cellular uptake was not inhibited by folic acid or MET as well as a lack of docking in the active sites. Another probable reason for increased cytotoxicity could be the efficient interaction of MET-F-MWCNT with the MET target, dihydrofolate reductase (DHFR). As observed with other receptor/carrier proteins, MET-F-MWCNT and MET-F-linker interactions with DHFR, probed by docking studies, were also inefficient (Figure 6E). The binding poses of MET-F-linker were not superimposable on binding conformation in the DHFR crystal structure (PDB entry 1U72) (Figure 6F). Ligand-based virtual screening of MET-F-linker was also performed to confirm observations in structure-based virtual screening (docking studies). Multiple conformations of MET-F-linker superimposed on DHFR-bound conformation of MET also revealed the inability of MET-F-linker to attain the desired

conformation (Figure 6G). Similar observations were also encountered, while comparing crystal/docked conformations of MET in FR α , FR β , RFC, and PCFT with MET-F-MWCNT and MET-F-linker by ligand-based virtual screening (data not shown). Molecular dynamics (MD) simulations were performed to further verify the observations in structure-based and ligand-based virtual screening methods. MD simulations revealed that MET-F-linker docked in the active site of DHFR (Figure 6H) moved out of the binding pocket (Figure 6I). Root mean square deviation (RMSD) analysis of MD trajectories over 20 ns revealed that dissociation of the MET-F-linker was very fast, and a near plateau was observed in 6 ns (Figure 6J; Video S1).

CNTs are known to interact with a wide range of tissues, and small changes in surface chemistry can have a profound effect on cell–CNT interactions culminating in alterations in therapeutic and toxicological profiles. Although our knowledge on *in vitro* and *in vivo* toxicity of CNTs continues to expand, there is still a dearth of understanding of the molecular mechanisms involved in cell–CNT interactions. Therefore, it becomes imperative to decipher and understand the biomolecular mechanisms that dictate cell–CNT interactions. Experimental demonstration of molecular (=receptor/transporter proteins) interactions with CNTs are confounded by nonspecific protein binding with a CNT backbone; hence, computational methods could be a rescue. Molecular docking and molecular dynamics studies could be employed to understand protein–CNT interactions using crystal and solution structures of proteins or homology models but are limited by computational costs. Hence, pharmacophore-based models are rapidly growing, which compare the query molecule with a database of known ligands for a given protein and, based on comparison of structural features between query molecule and database, determine the ability of the query ligand to interact with a set of proteins. PharmMapper is the largest pharmacophore database that screens the query molecule by comparing it with a database of known pharmacophores and identifies potential protein targets (receptors, enzymes, etc.). The data set consists of 23 236 proteins corresponding to 16 159 druggable pharmacophore models and 52 431 pharmacophore models, which screen the query molecule against 450 indications and 4800 molecular functions.^{55,56,61} The top 20 targets identified by PharmMapper did not include receptors or transporters involved in folate or MET uptake, thus complementing observations from

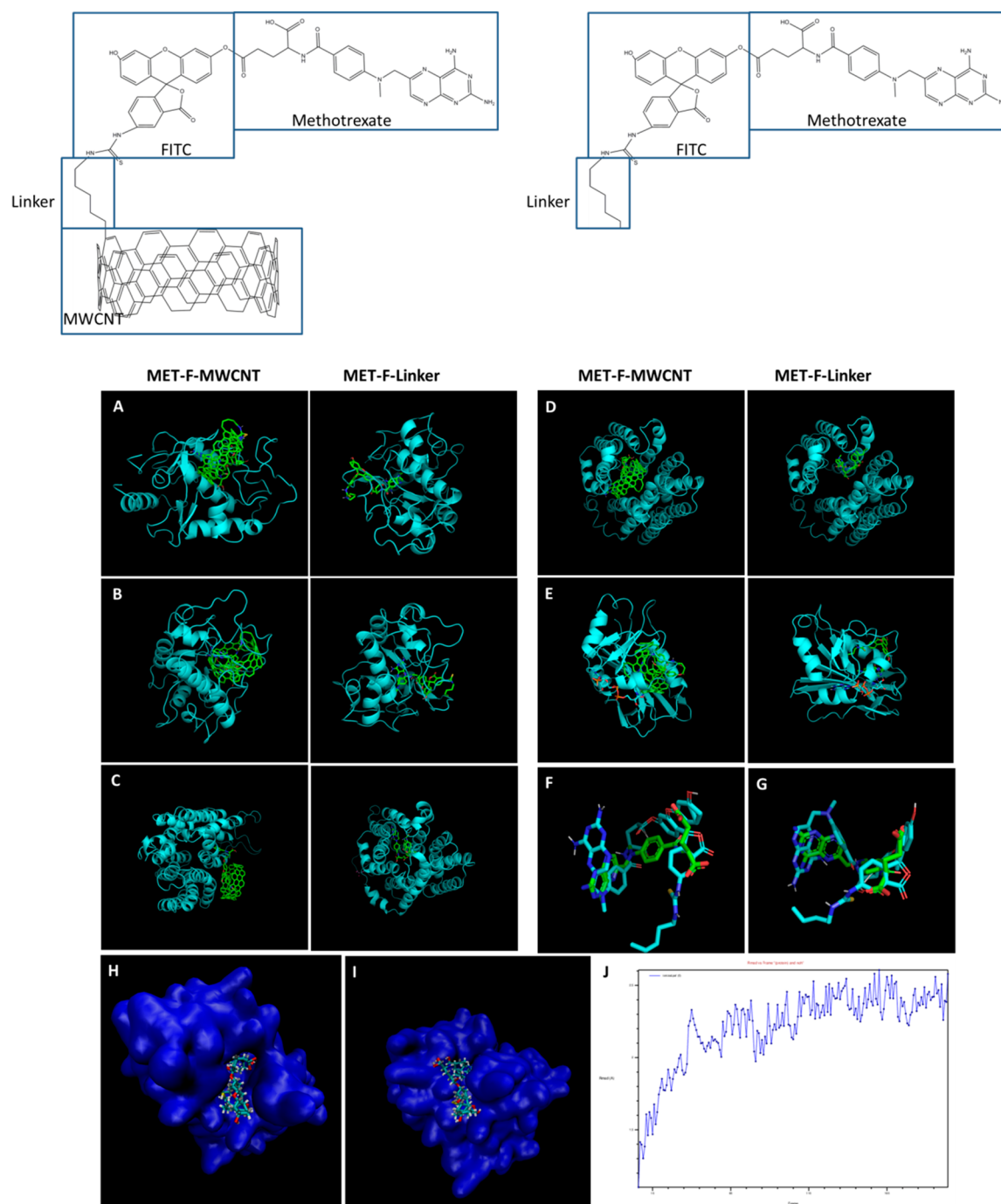


Figure 6. Docking of MET-F-MWCNT in folate receptor α (A), folate receptor β (B), reduced folate carrier (C), proton-coupled folate transporter (D), and dihydrofolate reductase (E). The left and right panels show docking results for MET-F-MWCNT and MET-F-linker, respectively. The structure of MET-F-MWCNT and MET-F-linker is shown at the top. Panel F shows a comparison of conformation of MET in DHFR (PDB entry 1U72) and docked conformation of MET-F-linker in panel A. (G) Ligand similarity of MET-F-linker with DHFR-bound conformation of MET in DHFR (PDB entry 1U72). Molecular dynamics simulation of the interaction of DHFR at the start of the simulation (H) and after 20 ns of simulation (I). (J) RMSD plot of molecular dynamics simulation (1 frame = 0.1 ns).

docking studies that MET-F-MWCNT (and MET-F-linker) does not interact with folate or MET carriers. Further, most of the pharmacophores identified by PharmMapper were comparable in MET-F-MWCNT and F-MWCNT, suggesting that the MWCNT portion is the major interacting moiety. The detailed results of druggable pharmacophore models for F-MWCNT and MET-F-MWCNT can be assessed in [Data S1 and S2](#), respectively. The detailed results of pharmacophore models for F-MWCNT and MET-F-MWCNT can be assessed

in [Data S3 and S4](#), respectively. The noninvolvement of folate transporters in uptake was further corroborated by observations that the cellular uptake of F-MWCNT and MET-F-MWCNT was comparable in a range of cell lines ([Figure 5B](#)). Therefore, the cellular uptake of MWCNTs in A549 cells appears to be mediated by a mechanism distinct from that involved in folate/MET uptake. Further, the addition of CNTs in the culture medium could result in the formation of protein corona on the CNT surface due to the sorption of proteins

from FBS, which could also interfere with the interaction of MET with receptor/transporter proteins.^{86,87}

Biological Activity of Drug Conjugate and Modulation by Dextran Sulfate. RES uptake is a stumbling block in the successful therapeutic application of NPs since this phenomenon decreases bioavailability at the target site with a concomitant increase in drug concentration in RES organs. The magnitude of this issue assumes even more importance when cytotoxic compounds are sequestered in RES, thereby implicating a need to rein in on the potential untoward effects in these organs. Therefore, as the first step, quantitative uptake of MET-F-MWCNT and DS@MET-F-MWCNT with the supramolecular assembly of DS (DS@MET-F-MWCNT) was compared in A549 cells and a macrophage cell line (RAW 264.7). Quantitative cellular uptake revealed a significantly higher cellular uptake of MET-F-MWCNT in RAW 264.7 cells compared to A549 cells. This observation is in line with the natural functions of macrophages, efficient engulfment of foreign bodies. In contrast, cellular uptake of DS@MET-F-MWCNT in RAW 264.7 cells was significantly reduced, while a small, but insignificant, increase in uptake was observed in A549 cells (Figure 7). Cytotoxicity was determined by an

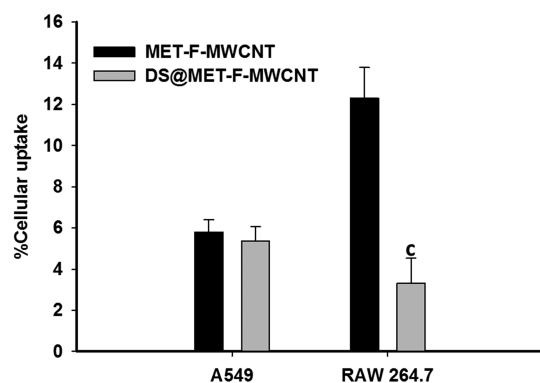


Figure 7. Quantitative cellular uptake of MET-F-MWCNT and DS@MET-F-MWCNT in A549 and RAW 264.7 cells. Cells were incubated with 100 $\mu\text{g}/\text{mL}$ of MET-F-MWCNT and DS@MET-F-MWCNT for 6 h, and cellular uptake was determined spectrophotometrically. Data is the mean \pm SD of 3–5 samples per treatment group. ^c $p < 0.001$ compared to MET-F-MWCNT in the same cell line by the *t*-test.

MTT assay to verify if the changes observed in cellular uptake also translate into toxicity in A549 and RAW 264.7 cells. The IC_{50} values of MET-F-MWCNT and DS@MET-F-MWCNT were found to be similar in A549 cells (15.8 ± 2.6 nM and 11.4

± 2.6 nM, respectively), while a significant ($p < 0.05$; *t*-test) increase in IC_{50} was observed in RAW 264.7 cells after DS functionalization (25.6 ± 3.5 nM versus 135 ± 20.2 nM). These results corroborate and verify cell uptake data, whereby a decrease in cell uptake is expected to decrease cytotoxicity (or increase IC_{50}).

Biological Activity of the Drug Conjugate with Suramin and DS. Motivated by the above results, we sought to combine the chemosensitizer and the stealth agent in a single system with real-time drug release monitoring properties. The rationale here was to develop a system that exhibits synergistic enhancement of drug activity together with a reduction in RES uptake. An obvious issue that can arise during simultaneous supramolecular functionalization with both agents is competition for binding on the MWCNT surface, culminating in lower efficiency of the binding process for both agents due to lesser availability of surface area and displacement. This could, at least theoretically, lower the overall efficiency of supramolecular functionalization of one or both of these agents. Hence, there is a need to optimize the concentration/proportion of both these agents such that a balance between synergistic enhancement of anticancer activity by SU in A549 cells and a decrease in cellular uptake by RAW 264.7 cells is achieved.

Traditional approaches applied in such conditions involve varying one parameter at a time (concentration of one agent), while other parameters remain constant (concentration of the second agent in this case). This one-factor-at-a-time (OFAT) approach has been challenged in recent years due to its oversimplification of the processes and limited relevance to the complex processes occurring under real-life situations. The design of the experiment (DOE) approach has been developed as an effective alternative to OFAT approaches, which allows simultaneous variations in two or more parameters to develop a mathematical model describing the multiparameter complex processes. The popularity and relevance of DOE can be gauged from the fact that the United States Food and Drug Administration and several other regulatory agencies have mandated quality by design (QbD) approaches for regulatory submissions.^{79,81} The umbrella term QbD comprises a plethora of approaches of which DOE is an important component. Therefore, we optimized the concentration of SU and DS using response methodology, a method of DOE.⁸⁰ The objective was to determine a concentration of SU and DS with an aim to maximize cytotoxic activity in A549 cells and minimize cellular uptake in RAW 264.7 cells. The concentration of both agents was varied between 1 and 10 mg/mL, while the MET-F-MWCNT concentration and total volume were kept constant

Table 4. Model Fitting Parameters of Response Surface Methodology^a

model type	SD	R ²	cytotoxicity (fold change)				
			adjusted R ²	predicted R ²	PRESS	BIC	AICc
linear	0.3689	0.8250	0.7901	0.6368	2.82		
2FI	0.3251	0.8777	0.8369	0.5852	3.23		
quadratic	0.1169	0.9877	0.9789	0.9603	0.3088	−11.57	−0.9563
				Cellular Uptake (%)			
linear	1.05	0.8660	0.8392	0.7528	20.42	42.49	43.46
2FI	1.11	0.8664	0.8218	0.5692	35.58		
quadratic	1.17	0.8845	0.8020	0.0200	80.94		

^aAbbreviations: SD = standard deviation; PRESS = predicted residual error sum of squares; BIC = Bayesian information criterion; AICc = corrected Akaike information criterion; 2FI = two-factor interaction

at 1 mg/mL and 10 mL, respectively. The cytotoxicity of SU and DS cofunctionalized MET-F-MWCNT (DS+SU@MET-F-MWCNT) in A549 cells was expressed as fold change (=fold increase) compared to MET-F-MWCNT (without SU) at a single concentration of 20 $\mu\text{g}/\text{mL}$ DS+SU@MET-F-MWCNT. Similarly, cellular uptake of DS+SU@MET-F-MWCNT in RAW 264.78 cells was expressed as a percentage of DS+SU@MET-F-MWCNT uptake at 20 $\mu\text{g}/\text{mL}$. The screening was performed at a single DS+SU@MET-F-MWCNT concentration because the statistical model allows only one value to be added per response parameter (one value each for cytotoxicity and cellular uptake) for every factor combination (different blends of SU and DS). The concentration of 20 $\mu\text{g}/\text{mL}$ was selected since it provided a significant signal to determine cytotoxicity and cellular uptake.

The model fitting parameters are shown in Table 4, and lack-of-fit statistics are shown in Table 5. As observed in Table

Table 5. Lack-of-Fit Parameters of Response Surface Methodology

cytotoxicity (fold change)				
model type	sum of squares	mean square	F-value	p-value
linear	1.35	0.2246	67.64	0.0006
2FI ^a	0.9379	0.1876	56.50	0.0008
quadratic	0.0824	0.0275	8.28	0.0344
Cellular Uptake (%)				
linear	10.04	1.67	6.50	0.0457
2FI ^a	10.01	2.00	7.78	0.0345
quadratic	8.51	2.84	11.03	0.0210

^a2FI = Two-factor interaction.

4, the quadratic model was apparently the best-fit model to describe the enhancement of cytotoxicity by SU due to the

highest R^2 value and lowest standard deviation. The model fitting, analyzed by analysis of variance (ANOVA), resulted in an F-value of 112.38 and $p < 0.0001$ with an adequate precision of 31.105, suggesting an excellent model fitting. This is further corroborated by the lowest sum of squares and F-value along with the highest p -value in the quadratic equation in lack-of-fit tests (Table 5). Similarly, the linear model best described the reduction in cellular uptake by DS (Tables 4 and 5). ANOVA revealed an F-value of 32.32, $p < 0.0001$, and adequate precision of 31.042, suggesting excellent model fitting. The response surfaces are shown in Figure 8A,B.

The correlation between concentration of both agents and cytotoxicity/cellular uptake was described by following equations:

cytotoxicity (fold change)

$$= 0.491 + 0.437 \times \text{SU} + 0.174 \times \text{DS} - 0.016 \times \text{SU} \times \text{DS} - 0.014 \times \text{SU}^2 - 0.014 \times \text{DS}^2$$

cellular uptake (%)

$$= 12.822 - 0.126 \times \text{SU} - 0.741 \times \text{DS}$$

where SU and DS represent the concentration of SU and DS in mg/mL, respectively.

Optimization of the statistical model was performed under two constraints: maximization of cytotoxicity in A549 cells and minimization of cellular uptake in RAW 264.7 cells. As expected on theoretical considerations, cofunctionalization of MET-F-MWCNT with DS and SU resulted in a decrease in cytotoxicity in A549 cells as well as an increase in uptake by RAW 264.7 cells. In none of the solutions obtained, the cytotoxicity in A549 cells or reduction in cellular uptake in RAW 264.7 cells was comparable to that obtained with SU alone (3.5-fold increase) or DS alone (3.3%), respectively. The

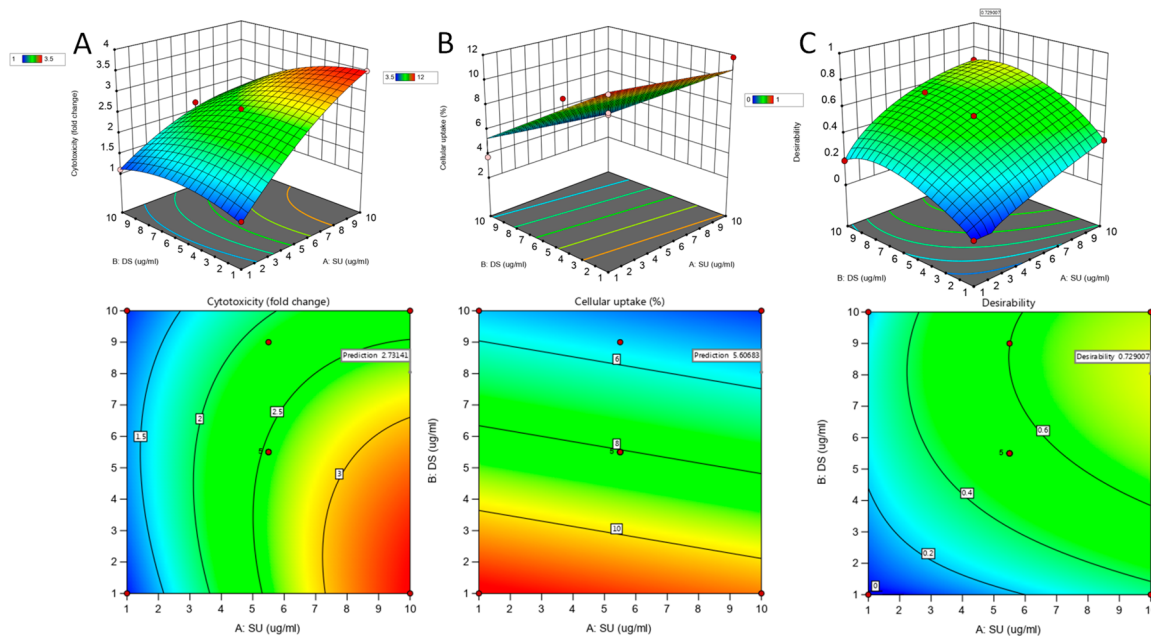


Figure 8. Response surface methodology for the effect of SU and DS concentrations on cytotoxicity in A549 cells (A) and cellular uptake in RAW 264.7 cells. Panel C shows the desirability of the model at different SU and DS concentrations. The upper panel shows data as a three-dimensional surface plot, and the lower panel shows the same data in the two-dimensional contour plot. Cells were incubated with 20 $\mu\text{g}/\text{mL}$ of DS+SU@MET-F-MWCNT, and cytotoxicity was determined by the MTT assay after 72 h incubation, while cellular uptake was determined spectrophotometrically after 6 h of incubation.

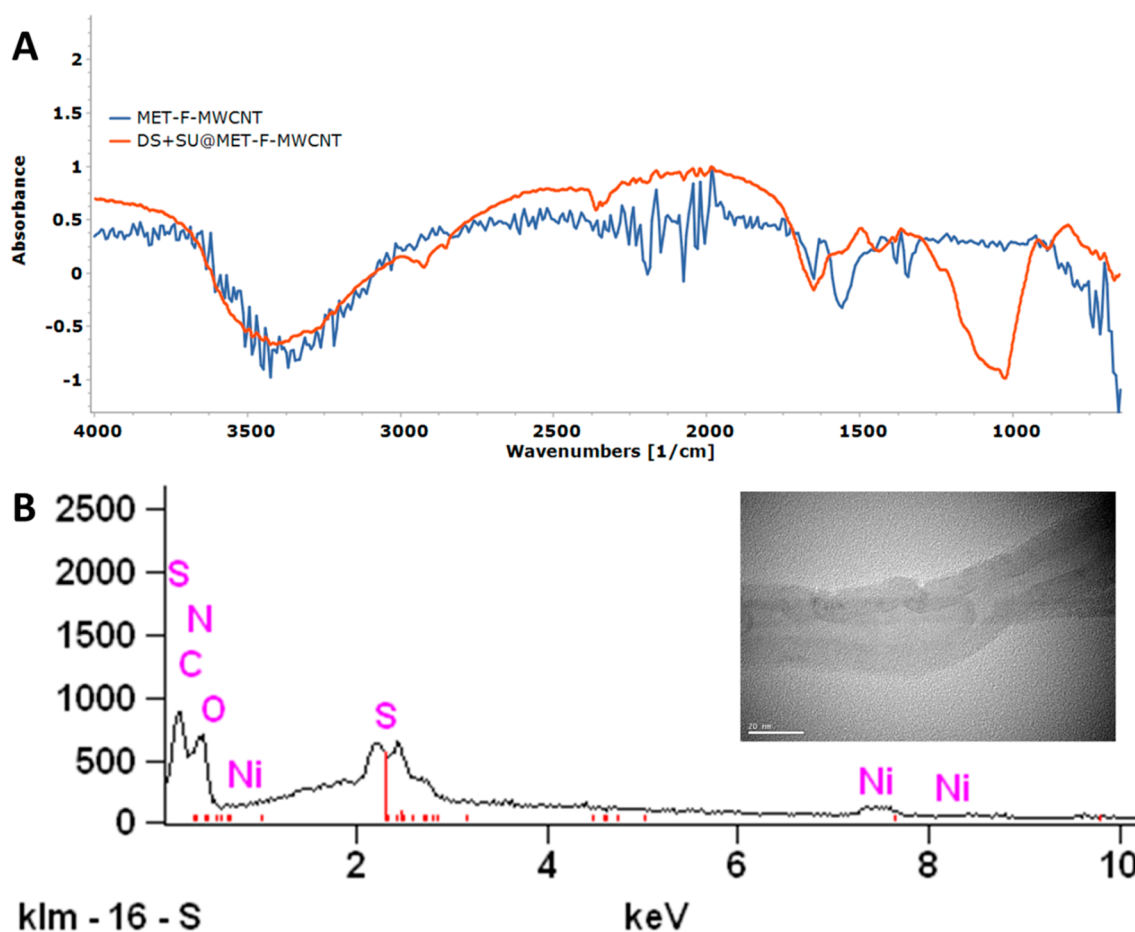


Figure 9. Characterization of DS+SU@MET-F-MWCNT by ATR-FTIR (A) and EDX (B). Inset shows the HRTEM image of DS+SU@MET-F-MWCNT.

optimized concentrations were determined using the desirability function, which ranges between 0 and 1, where desirability values close to 1 indicate ideal values. The highest desirability value was found to be 0.73 for a combination containing 10 mg/mL SU and 8.1 mg/mL DS, which resulted in a 2.7-fold increase in cytotoxicity in A549 cells compared to MET-F-MWCNT and cellular uptake of 5.6% (55% reduction compared to MET-F-MWCNT; 170% higher compared to DS@MET-F-MWCNT). The desirability values at different SU and DS ratios are shown in Figure 8C. The model was further confirmed by postanalysis, whereby three independent data points were evaluated and found to exhibit good fit ($p < 0.0001$).

Physicochemical characterization of the optimized formulation revealed SU and DS loading of 0.08 mg SU and 0.15 mg DS per mg of DS+SU@MET-F-MWCNT. This was confirmed by ATR-FTIR, which revealed a peak around 1000 cm^{-1} , corresponding to the α -glucan moiety in DS. This peak overlaps with the S–O stretching vibration of SU. Further, the amide band of SU around 1550 cm^{-1} also overlaps with the amide band of MET. Hence, the two characteristic IR features of SU were obscured by co-loaded molecules. Energy-dispersive X-ray spectroscopy also revealed a predominant S $K\alpha$ peak corresponding to sulfate groups present in DS and SU. The Ni peaks correspond to the residual heavy metal present in MWCNTs and contribute to $<1\%$ w/w of MWCNTs.

HRTEM analysis revealed the structure of MWCNT was not altered during the preparation steps (Figure 9).

The *in vitro* rate of hydrolysis of DS+SU@MET-F-MWCNT was comparable ($p > 0.05$; one-way ANOVA followed by Tukey's test) with MET-F-MWCNT in PBS and A549 cells (0.2 ± 0.0 vs 0.2 ± 0.0 and 0.6 ± 0.2 vs 1.1 ± 0.1 $\Delta F/\text{min}$, respectively) but significantly lower ($p < 0.001$) in A549 lysates (4.6 ± 0.5 vs 6.0 ± 0.6 $\Delta F/\text{min}$). The mechanism of cellular uptake was determined by coincubation of DS+SU@MET-F-MWCNT with inhibitors of active uptake (4°C , sodium azide), clathrin- (CPZ) and caveolin-mediated endocytosis (HPbCD). Cellular uptake was significantly inhibited by all inhibitors suggesting an active uptake mechanism involving clathrin- and caveolin-mediated endocytosis. Considering the length of MWCNTs ($\sim 20\ \mu\text{m}$) and incomplete inhibition of cellular uptake by endocytosis inhibitors, the role of other mechanisms, such as phagocytosis or macropinocytosis, also appears plausible.⁷⁷ Further, confocal microscopy revealed cytosolic localization of the formulation, suggesting that MET is released in the cytoplasm (Figure 10A). A closer examination of the confocal image revealed that the cytoplasmic fluorescence was diffused in nature, suggesting that CNTs are not localized in cell organelles since lysosomal or mitochondrial localization results in the punctuate appearance of fluorescence. The cytoplasmic distribution of CNTs was restricted to the perinuclear region since the fluorescence from CNT (green fluorescence due to fluo-

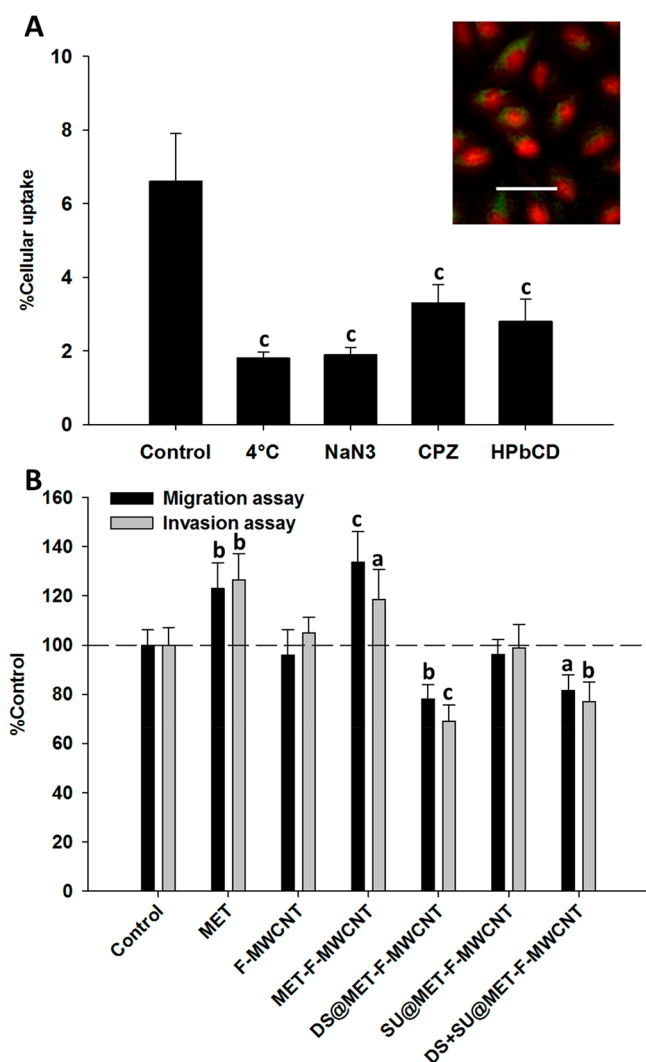


Figure 10. (A) Quantitative cellular uptake of DS+SU@MET-F-MWCNT in the presence of inhibitors of active uptake (4 °C, sodium azide), clathrin- (CPZ) and caveolin-mediated endocytosis (HPβCD). Inset shows a confocal micrograph of cells after 6 h incubation showing cytosolic localization of MWCNTs (green fluorescence due to F-MWCNT); red fluorescence shows the nucleus (propidium iodide). (B) *In vitro* cell migration and cell invasion assay of free MET and CNT conjugates. Scale bar = 50 μm A549 cells were incubated with 100 μg/mL of DS+SU@MET-F-MWCNT for 6 h, and cellular uptake was determined spectrophotometrically. Data is the mean ± SD of 5–6 samples per treatment group. A549 cells were incubated with MET (1 μM) or an equivalent amount of MET-F-MWCNT, DS @MET-F-MWCNT, SU@MET-F-MWCNT, and DS +SU@MET-F-MWCNT for 24 h. The F-MWCNT concentration was 50 μg/mL. Cell migration was determined in uncoated transwells, while cell invasion was determined in collagen-coated transwells. Data is the mean ± SD of 4–6 samples per treatment group. **p* < 0.05, ^b*p* < 0.01, ^c*p* < 0.001 compared to the control by one-way ANOVA followed by *post hoc* Tukey's test. NaN₃ = Sodium azide, CPZ = chlorpromazine, HPβCD = hydroxypropyl-*b*-cyclodextrin.

rescein) did not overlay with the nuclear fluorescence (red fluorescence from a nuclear stain, propidium iodide). These results suggest that, following uptake, DS+SU@MET-F-MWCNT is trafficked to the cytosolic compartment where MET is hydrolyzed.

Methotrexate is approved for the treatment of breast cancer and lymphoma in addition to lung cancer. Therefore, the

activity of DS+SU@MET-F-MWCNT in cell lines representing lung cancer (A549), breast cancer (MCF-7), and lymphoma (MOLT-4) was determined. Cell viability analysis by the MTT assay, following incubation with DS+SU@MET-F-MWCNT, exhibited IC₅₀ values of 7.7, 41.5, and 3.6 nM in A549, MCF-7, and MOLT-4 cells, respectively. These values were slightly lower than those observed with SU@MET-F-MWCNT but were comparable (*p* > 0.05; ANOVA). On the other hand, these values were about 2-fold lower compared to MET-F-MWCNT and over 3-fold higher compared to free MET (Table 2). Similarly, oxidative DNA damage and p53 levels in A549 cells were increased to 2.0- and 1.6-fold compared to the control, while the PCNA level was decreased to 0.6-fold compared to the control. These values are comparable to those observed in SU@MET-F-MWCNT (*p* > 0.05; *t*-test) (Table 3). In contrast to these, the IC₅₀ value of the conjugate was increased in RAW 264.7 cells (128 ± 14.8 nM) compared to MET-F-MWCNT (25.6 ± 3.5 nM) but was comparable to DS@MET-F-MWCNT (135 ± 20.2 nM).

DS has been shown to inhibit metastasis and endothelial–mesenchymal transition transformation under *in vitro* and *in vivo* conditions,^{88,89} similar to those observed in other polyanionic SR ligands.⁹⁰ This inhibitory action of DS could be attributed, at least in part, to inhibition of SR-binding properties.⁹¹ Therefore, it appears plausible that DS+SU@MET-F-MWCNT could inhibit cell migration in an *in vitro* assay. Transwell migration and invasion assays are commonly employed to mimic *in vivo* cell migration;⁵³ hence, these assays were adopted. As expected, DS@MET-F-MWCNT and DS +SU@MET-F-MWCNT significantly reduced cell migration and cell invasion. DS@MET-F-MWCNT appeared to be relatively more effective in reducing cell migration and invasion compared to DS+SU@MET-F-MWCNT, but the difference was insignificant (*p* > 0.05) in both assays. In contrast, MET and MET-F-MWCNT appeared to slightly increase migration and invasion of A549 cells (Figure 10B). This is in agreement with earlier studies demonstrating an increase in the invasiveness of A549 cells following MET treatment.^{92,93} Numerous studies have documented the role of alternatively activated M2 macrophages in cancer and are commonly known as tumor-associated macrophages (TAMs). These macrophages produce anti-inflammatory molecules and help in cancer survival and tissue invasion. Due to their central role in cancer survival, TAMs have emerged as an important therapeutic target in recent years.^{94,95} TAMs highly express an SR, CD163, and the specific expression of this receptor has been exploited as a molecular marker for TAM identification.^{94,95} Additionally, TAMs have also been demonstrated to express SR-A and MARCO at higher levels compared to normal macrophages, and their inhibition has been related to cancer regression in animal models.^{96–98} The multitude of potential molecular and cellular targets in tumors, along with RES evading properties, affirms the potential of DS as an adjuvant in novel drug delivery systems for tumor therapy.

A pertinent question that arises here is if DS and SU adsorbed on MET-F-MWCNT are desorbed under physiological conditions. To answer this question, the desorption of DS and SU was determined in A549 cell lysates. Fluorescence measurements revealed no detectable sorption of SU on MWCNTs recovered after 6 h of incubation in A549 cell lysates, while >90% SU was observed in the lysates. DS does not possess fluorescent properties, which posed a major problem in analysis. The high molecular weight (>500 000 Da)

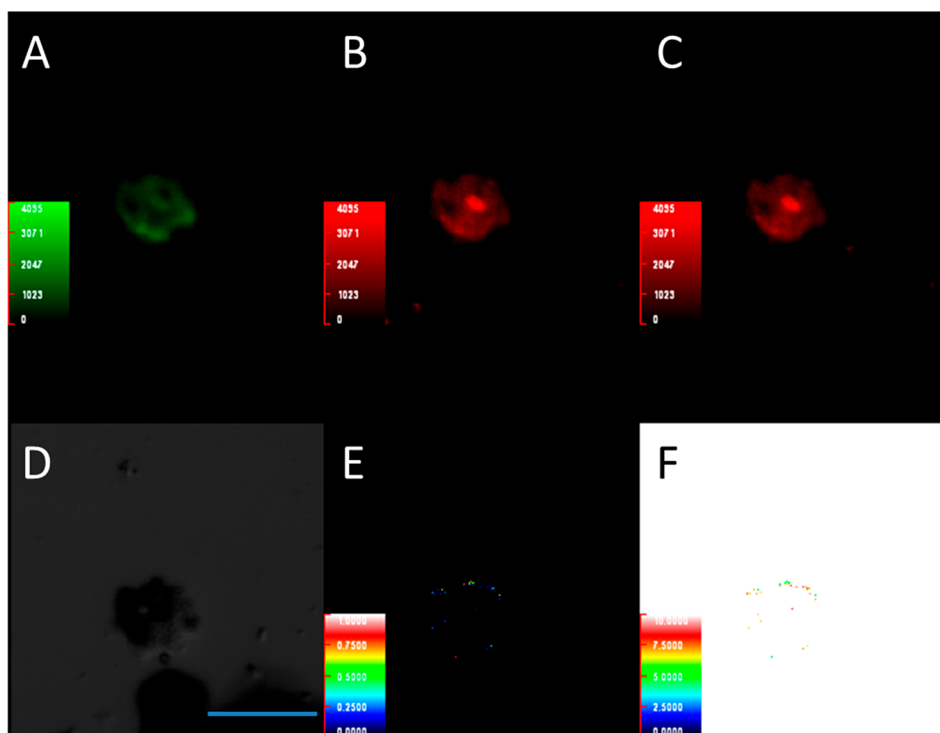


Figure 11. Interaction between fluorescein-labeled DS and rhodamine-labeled MWCNTs determined by FRET. (A) Fluorescein (donor) fluorescence after excitation of the donor, (B) rhodamine (acceptor) fluorescence after excitation of both donor and acceptor excitation, (C) acceptor fluorescence following excitation of the acceptor, and (D) differential interference contrast image of MWCNT. Panel E shows FRET efficiency at different locations on the MWCNT agglomerate, while panel F shows the distance between donor and acceptor at different locations. FRET is noticed only at the edges of the bundle due to fluorescence quenching in the bulk of MWCNTs. Scale bar = 50 μm

combined with low concentration made reliable quantification by extraction of DS impractical due to losses during the extraction and sample derivatization procedures (required for chromatographic detection). Therefore, DS was labeled with DTAF (DS-DTAF) to enable easy, reliable, and sensitive detection of DS. Preliminary studies suggested that SU loading was approximately 6% lower when DS-DTAF was used instead of DS. Fluorescence measurements revealed nearly one-fourth (28%) of DS-DTAF was detectable on MWCNTs, and nearly one-third (67%) was detectable in the cell lysate. The binding of DS to CNTs was also confirmed by FRET using fluorescein (DS-DTAF) as a donor and rhodamine (RBITC-labeled amino-functionalized MWCNTs) as an acceptor. The recovered MWCNTs exhibited FRET when observed under a fluorescence microscope (Figure 11), corroborating fluorescence data indicating sorption of DS-DTAF on MWCNTs. Desorption measurements performed in the culture medium revealed that <10% of SU and DS-DTAF were released in the culture medium after 6 h of incubation while <5% of both sorbents were released in water over the same duration.

The nature of interactions between CNT and DS/SU was studied using MD simulations. Although MWCNTs were used in the present experiments, MD simulations were performed using a single-walled CNT (SWCNT). This simplification was adopted to reduce the total number of atoms in simulation and the computational cost. This is because modeling an MWCNT would increase the number of CNT atoms by several orders of magnitude, and a 30–50-mer saccharide was required instead of the decamer used in the current study. A corresponding increase in the water box size and the number of water molecules was also required. We believe that this simplification does not have a significant bearing on the nature of

interactions because the chemical composition of the CNT surface is similar in SWCNT and MWCNT. Based on 50 ns of MD simulations, both DS and SU were found to interact with CNTs through specific and directional π - π stacking interactions (Figure 12A,B; Figure S2; Videos S2 and S3). DS binds to CNT through one of its ends, as the molecule is stiff enough that the entropic penalty to completely bind the CNT is too large. The average distance of each of the 10 residues, averaged over the last 10 ns of the simulation, is shown in Figure 12C, while the average angle between the axis of the CNT and the vector normal to the monosaccharide ring is shown in Figure 12D. The residues are ordered from adjacency to CNT; i.e., residue 1 is nearest to the CNT surface, and residue 10 is the farthest. The distance and angle to the CNT over the entire simulation run (50 ns) are shown in Figure S3. It is interesting to note that, once residue 1 binds to the CNT surface, it does not unbind. The mode of interaction appears to be π - π stacking interactions since the distance between two adjacent planes (aromatic rings in CNT and monosaccharide units in DS) is lower than 4.8 Å, and the angle between the axis of the CNT and the vector normal to the hexagonal ring is within $90 \pm 30^\circ$. These results suggest that DS can tether to the CNT surface, and the polysaccharide chain could extend into the aqueous environment. In the case of longer polysaccharide chains, it is expected that the polysaccharide chain would form coils to attain thermodynamic stability and thus interact with CNTs via a wrapping mechanism, which is in agreement with previous atomic force microscopy results.⁹⁹

MD simulations of SU showed that, unlike DS, which binds from one end, SU tends to bind CNT from the middle. Residues 1 and 8 are the disulfonated aromatic rings, and

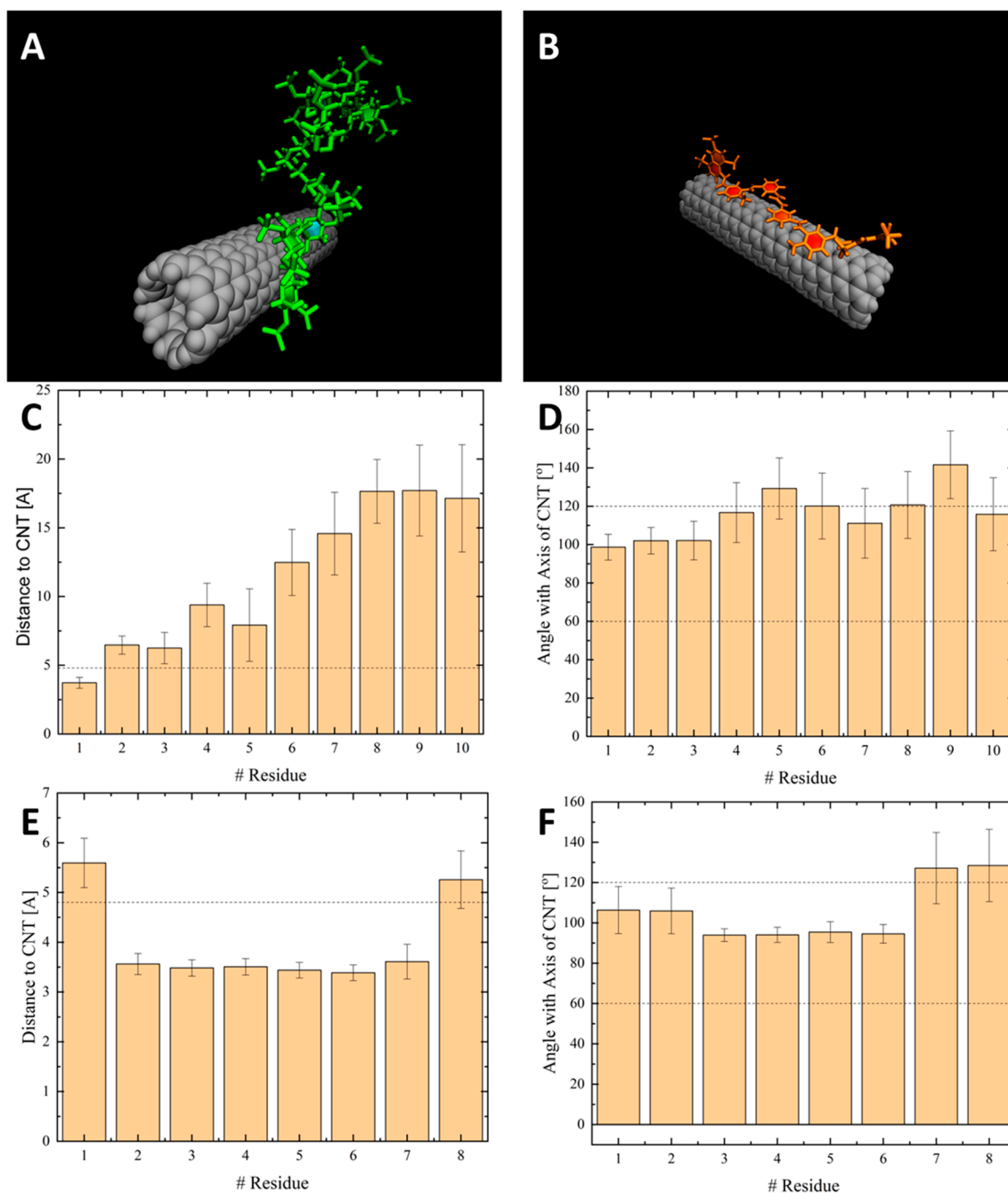


Figure 12. MD simulations showing the interaction of CNTs with dextran sulfate (DS) and suramin (SU). (A) Binding configuration of DS+ CNT. (B) Binding configuration of SU + CNT. The conformations of these molecules are shown after 50 ns of equilibration near CNTs. Note that the CNTs are uncharged; however, molecules containing aromatic groups, like DS and suramin, are capable of achieving noncovalent functionalization by forming specific and directional π - π stacking interactions. (C) Average distance of the residues of DS to the CNT (average performed over the last 10 s). (D) Average angle between the axis of the CNT and the vector normal to the hexagonal ring of DS (average performed over the last 10 s). (E) Average distance of the residues of SU to the CNT (average performed over the last 10 s). (F) Average angle between the axis of the CNT and the vector normal to the hexagonal ring of SU (average performed over the last 10 s). A (6,6) CNT (length 36.9 Å and diameter 8.1 Å) was solvated in a $50 \times 50 \times 50 \text{ \AA}^3$ box with TIP3P water and sodium ions to neutralize the charge. The system was equilibrated for 125 000 steps (2 fs/step; NVT ensemble) followed by simulation for 50 ns using the NPT ensemble at 310.15 K. DS was modeled as a decamer, and simulation was performed using NAMD and the CHARMM36 force field.

residues 2 and 7 are the monosulfonated aromatic rings of the naphthalene moieties. The other rings are numbered serially, moving from one end (residue 1) to the other end (residue 8) of the SU molecule. SU was also found to interact with CNTs via π - π interactions since the distance between two adjacent aromatic planes (aromatic rings in CNT and aromatic rings in SU) is lower than 4.8 Å, and the angle between the axis of the

CNT and the vector normal to the aromatic ring is within $90 \pm 30^\circ$ (Figure 12E,F; Figure S4). A similar π - π stacking mechanism of interaction has been reported in other aromatic compounds as well.^{100,101} An interesting observation in SU was that the residues 1 and 8 (disulfonated aromatic ring in the naphthalene systems) did not effectively interact with the CNT surface since the distance was $>5 \text{ \AA}$ and the angles were

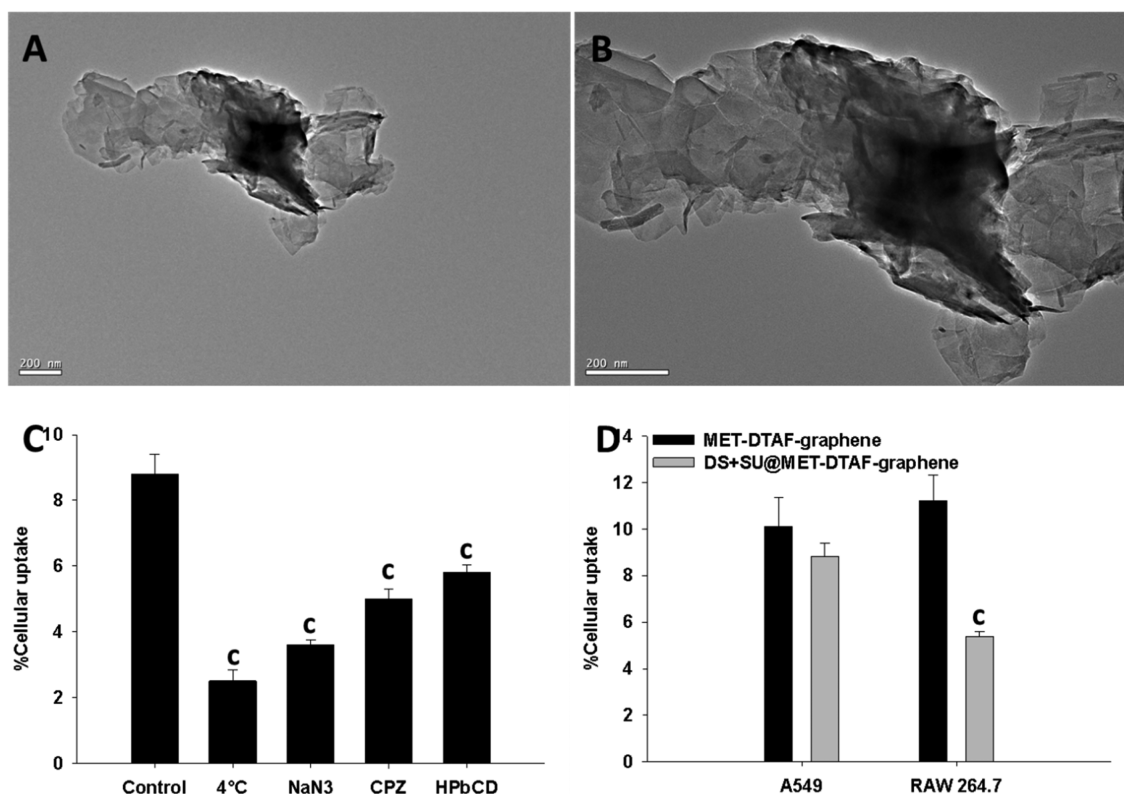


Figure 13. (A) HRTEM image of DS+SU@MET-DTAF-graphene at a low magnification. Panel B shows the same field at a higher magnification. (C) Quantitative cellular uptake of DS+SU@MET-F-MWCNT in the presence of inhibitors of active uptake (4 °C, NaN₃), clathrin- (CPZ) and caveolin-mediated endocytosis (HPβCD). (D) Quantitative cellular uptake of MET-DTAF-graphene and DS+SU@MET-DTAF-graphene in A549 and RAW 264.7 cells. Cells were incubated with 100 μg/mL of indicated conjugates, in the absence (control) or presence of inhibitors, for 6 h, and cellular uptake was determined spectrophotometrically. Data is the mean ± SD of 5–6 samples per treatment group. **p* < 0.001 compared to the control by one-way ANOVA followed by *post hoc* Tukey's test in panel C. †*p* < 0.001 compared to MET-DTAF-graphene in the same cell line by *t*-test (D). NaN₃ = Sodium azide, CPZ = chlorpromazine, HPβCD = hydroxypropyl-*b*-cyclodextrin.

relatively higher for the two naphthalene rings compared to the phenyl rings (residues 3–6). This may be attributed to the anionic character on the naphthalene rings (due to sulfonation), which results in repulsion between electron-rich aromatic rings of CNTs and the anionic naphthalene rings. This is further supported by π - π interaction mapping of DS and SU with CNTs (Figure S5). Apart from the differences in binding modes of DS (binding from one end) and SU (binding from the middle) on the CNT surface, another interesting difference between the nature of the interaction of these molecules with CNT was revealed by end-to-end distance measurements. The end-to-end distance of DS alone and in combination with CNT was comparable so that DS remains as a linear chain and its conformation is not significantly altered after binding to CNTs (Figure S6). This assertion is complemented by microscopic observations suggesting that DS with a molecular weight of 5 kDa (ca. 30 glucose residues) remains close to a linear molecule in water.⁹⁹ In contrast to DS, the end-to-end length of SU appears to increase the following binding with CNT. This suggests that SU tends to stretch along the CNT, presumably to maximize the number of π - π interactions between CNT and SU, resulting in a more stable complex. A similar phenomenon has also been reported in DNA sorbed on carbonaceous NPs^{86,87} and silicon oxide.¹⁰² RMSD plots of the two systems show that DS binding to CNT is relatively faster and that a stable conformation is reached in a few ns. On the other hand, SU binds relatively slowly, and the

system stabilizes after about 15 ns of simulation (Figure S7). The relatively faster association kinetics of DS could be explained by two observations in the MD simulation: first, DS binds on the CNT through one of its two ends, while SU binds via multiple sites, and second, DS behaves as a rigid molecule, while SU extends after binding to the CNT surface.

It may be argued that the MD simulations are an oversimplification of the processes occurring on the CNT surface in DS@MET-F-MWCNT, and under real-life situations, DS and SU could also interact, resulting in enhanced loading of SU. We conducted 150 ns MD simulations of a mixture of DS and SU and showed an insignificant interaction between DS and SU (Video S4 and Figure S8). In addition, the sorption of SU on DS-coated microtiter plates was tested experimentally to prove the assertion. Interestingly, >95% of SU was detected in solution, suggesting an insignificant interaction between DS and SU. These results provide circumstantial evidence that DS and SU bind to CNTs independently of each other. A plausible mechanism of coloaded DS and SU thus entails a wrapping mechanism of DS around CNTs, while SU may bind to the remaining unoccupied area on the CNT surface. Further, in the presence of DS, a molecularly crowded environment may not allow interaction of all aromatic rings of SU with CNT, but such lower degrees of interaction may not have an adverse impact on the overall loading efficiency of SU on the CNT surface. This is confirmed by the observation that SU and DS

Table 6. Hydrolysis and Cytotoxicity of Conjugates^a

conjugate	rate of hydrolysis ($\Delta F/\text{min}$)			IC ₅₀ (nM)		
	PBS	A549 cell lysate	A549 cells	A549	MCF-7	MOLT-4
free MET				35.6 ± 5.8	123.5 ± 11.0	14.6 ± 2.3
MET-DTAF-graphene (1.5) ^b	0.1 ± 0.0	5.5 ± 1.3 ^e	0.8 ± 0.1	25.5 ± 1.8 ^c	75.6 ± 8.1 ^c	7.8 ± 0.8
DS+SU@MET-DTAF-graphene (1.1) ^b	0.1 ± 0.0	3.8 ± 0.6 ^e	0.5 ± 0.1	11.3 ± 1.1 ^e	52.8 ± 3.3 ^e	3.5 ± 0.5 ^d

^aMET-DTAF-graphene and DS+SU@MET-DTAF-graphene were incubated in PBS, A549 cell lysate, or A549 cells, and fluorescence intensity was determined at regular intervals. The rate of hydrolysis is expressed as an increase in fluorescence intensity (arbitrary units) per minute. Cells were incubated with free MET or drug conjugates for 72 h, and cell viability was determined by the MTT assay. The IC₅₀ of drug conjugates is expressed in terms of the amount of conjugated MET added to cells. Data is the mean ± SD of 3–6 samples per treatment group. ^bValues in parentheses indicate the amount of MET (in μmol) per mg of the conjugate. ^c $p < 0.05$ with respect to hydrolysis in PBS by one-way ANOVA followed by *post hoc* Tukey's test. ^d $p < 0.01$ with respect to hydrolysis in PBS by one-way ANOVA followed by *post hoc* Tukey's test. ^e $p < 0.001$ with respect to hydrolysis in PBS by one-way ANOVA followed by *post hoc* Tukey's test.

loading was 0.08 mg and 0.15 mg per mg of DS+SU@MET-F-MWCNT compared to 0.10 mg of SU and 0.21 mg of DS per mg of SU@MET-F-MWCNT and DS@MET-F-MWCNT, respectively. Similar observations have also been reported with CNTs coloaded with chitosan with doxorubicin and paclitaxel on CNTs, whereby chitosan was shown to wrap around the CNT while doxorubicin and paclitaxel adsorbed on the remaining CNT surface.⁴⁸

Extension of the Real-Time Fluorescence Monitoring Platform to Other NPs. As outlined earlier, a large number of NP-based systems enabling real-time drug release monitoring have been developed but are at a disadvantage because not all drugs possess the desired physicochemical and fluorescent properties^{8,10–16} or the systems have been tailored for a single or extremely small range of compounds.^{17,18} However, the system described in this study has the potential to be extended to other types of NPs since the system only requires a free carboxylic group in the drug molecule. Therefore, graphene was chosen as another NP. Acid-functionalized graphene was conjugated with DTAF followed by esterification with MET. HRTEM images show that the structure of graphene was intact in MET-DTAF-graphene (Figure 13). DS+SU@MET-DTAF-graphene was prepared by mixing equal amounts of DS and SU (10 mg each) without following the elaborate response surface methodology. As observed in DS+SU@MET-F-MWCNT, coloaded of DS and SU on MET-DTAF-graphene resulted in a relative decrease in the rate of hydrolysis compared to unloaded MET-DTAF-graphene (Table 6). It seems plausible to assume that the long chains of DS could sterically hinder the access of cytoplasmic esterases to esterified MET, resulting in a decrease in the rate of hydrolysis in A549 cell lysates and in A549 cells. On the other hand, the activity of DS+SU@MET-DTAF-graphene was found to be significantly higher than MET-F-MWCNT or free MET. This increase in cytotoxicity could be attributed to increased cytosolic delivery of MET due to conjugation with graphene, along with the synergistic activity of SU (Table 6).

Quantitative uptake revealed that cellular uptake of DS+SU@MET-DTAF-graphene in A549 cells was mediated by an active process as evident from a decrease in uptake at a low temperature (4 °C) and in the presence of sodium azide. Further, inhibitors of clathrin- and caveolin-mediated uptake mechanisms also significantly inhibited cellular uptake, suggesting a major role of both pathways in cellular uptake. Additionally, cellular uptake of DS+SU@MET-DTAF-graphene was significantly lower ($p < 0.001$ by *t*-test) compared to uptake of MET-DTAF-graphene in RAW 264.7 cells. On the other hand, cellular uptake of DS+SU@MET-DTAF-

graphene and MET-DTAF-graphene was found to be comparable ($p > 0.05$ by *t*-test) in A549 cells (Figure 13). These observations are in accordance with those observed in DS+SU@MET-F-MWCNT, suggesting RES evading properties of DS+SU@MET-DTAF-graphene.

Expanding the Scope of the Real-Time Fluorescence Monitoring Platform to Other Diseases and Drugs.

CNTs and other NPs tend to accumulate in conditions with a leaky vasculature, such as cancer and inflammation, by a phenomenon called enhanced permeation and retention (EPR). EPR effect has been frequently employed for passive targeting NPs to tumors and inflammatory conditions and found to increase the availability of drug conjugates at such sites. Since MET is approved for an autoimmune disorder like arthritis and lupus, it seems logical to assume that MET-F-MWCNT could be used in such inflammatory conditions. It may be argued here that evasion of macrophage uptake, due to DS, could occur in resident tissue macrophages and infiltrating macrophages, resulting in a decrease in therapeutic response. We believe that this argument might not hold well because, even if the conjugates do not enter the cells, their concentration at the inflammation site will be higher than the concentrations achieved by the free drug. The extracellular hydrolysis of the ester bond could release the drug, resulting in an increased local concentration.¹⁰³ Additionally, DS acts as an inhibitor of pattern recognition receptors, notably the scavenger receptor-A (SR-A) and macrophage receptor with a collagenous domain (MARCO). Further, the presence of SU can also enhance the anti-inflammatory activity of MET due to the inhibition of purinergic receptors.

Another advantage that such a system will offer is the lower concentration at nontarget sites. For example, cetirizine, a commonly used antiallergic drug, possesses excellent blood–brain barrier penetration, which results in sedation due to central anticholinergic effects. Since CNTs, in the absence of a brain-targeting agent, could not enter the brain, it is expected that cetirizine conjugated to CNTs could not access the central nervous system and will concentrate at the inflammation site. Further, several drugs are actively metabolized by the liver and excreted quickly in urine, which results in a reduction in drug available in circulation. CNT–drug conjugates are expected to evade RES due to DS coating and urinary excretion due to their physical characteristics resulting in longer circulation time and hence lower dose requirements. We conjugated two nonsteroidal anti-inflammatory drugs (aspirin and mefenamic acid) and an antihistaminic drug (cetirizine) as support to the wider application of the platform described here. The *in vitro* hydrolysis results are presented in Table 7. *In vitro* drug release

in the presence of A549 cell lysate exhibited a linear correlation ($R^2 > 0.9$) between drug release and fluorescence intensity.

Table 7. Hydrolysis of Conjugates in Phosphate-Buffered Saline (PBS; pH 7.4), A549 Cell Lysate, and A549 Cells^a

conjugate	rate of hydrolysis ($\Delta F/\text{min}$)		
	PBS	A549 cell lysate	A549 cells
aspirin	0.2 \pm 0.0	4.9 \pm 0.5 ^c	1.1 \pm 0.1 ^b
mefenamic acid	0.2 \pm 0.0	1.9 \pm 0.1 ^c	1.2 \pm 0.1 ^b
cetirizine	ND	2.2 \pm 0.2 ^c	1.1 \pm 0.1 ^b

^aMET-F-MWCNT were incubated in PBS, A549 cell lysate, or A549 cells, and the fluorescence intensity was determined at regular intervals as described in the Materials and Methods section. The rate of hydrolysis is expressed as the increase in fluorescence intensity (arbitrary units) per minute. ND = Not detectable hydrolysis ($<0.1 \Delta F/\text{min}$). ^b $p < 0.05$ with respect to hydrolysis in PBS by one-way ANOVA followed by *post hoc* Tukey's test. ^c $p < 0.001$ with respect to hydrolysis in PBS by one-way ANOVA followed by *post hoc* Tukey's test.

In conclusion, we report a novel fluorescence turn-on theranostic platform based on MWCNTs in which the fluorescence is quenched due to the covalent linkage of drug molecules to the fluorophore via ester bonds. The hydrolysis of ester bonds by the action of intracellular esterases results in activation of fluorescence; the ensuing increase in fluorescence intensity correlates with the amount of drug released. Several diseases are characterized by overexpression of specific enzymes at the target site and a careful selection of drugs, fluorophores, and linkage bonds can aid in site-specific cleavage and delivery of the payload, while also allowing monitoring of drug release. Supramolecular functionalization with SU could increase the activity of anticancer compounds, while DS could evade RES, thereby suggesting their potential application as a chemoenhancer and a stealth agent, respectively. Although MWCNTs have been employed as model nanoparticles and MET as a model in the present study, the general chemistry reported here could be extended to other nanoparticles as well as exemplified by graphene. Similarly, the generic nature of the platform makes it amenable for the extension to other drugs and diseases. The platform is limited in application and may not be suitable for imaging of deep tissues due to scattering and quenching of fluorescence emission as well as interference due to autofluorescence arising from biomolecules. These issues could be addressed if fluorescein is replaced with a near-infrared-emitting dye.

■ ASSOCIATED CONTENT

SI Supporting Information

The Supporting Information is available free of charge at <https://pubs.acs.org/doi/10.1021/acs.molpharmaceut.0c00730>.

ATR-FTIR of amino-functionalized MWCNT, F-MWCNT, and MET-F-MWCNT; conformation of DS and SU after equilibration steps; distance and angle of residues of DS and SU to the CNT as a function of time; end-to-end distances of DS and SU; RMSD of DS-CNT, SU-CNT, and DS-SU systems (PDF)

Video S1 (MPG)

Video S2 (MP4)

Video S3 (MP4)

Video S4 (MPG)

Data S1 (XLSX)

Data S2 (XLSX)

Data S3 (XLSX)

Data S4 (XLSX)

■ AUTHOR INFORMATION

Corresponding Author

Raman Preet Singh – School of Pharmaceutical Sciences, Shoolini University, Solan, Himachal Pradesh 173 221, India; Department of Pharmacy, Government Polytechnic College, Bathinda, Punjab 151 001, India; orcid.org/0000-0002-2714-0068; Email: ramanpreetsingh@hotmail.com; Fax: +91-1792-308000

Authors

Arjun Attri – School of Pharmaceutical Sciences, Shoolini University, Solan, Himachal Pradesh 173 221, India

Deepak Thakur – School of Pharmaceutical Sciences, Shoolini University, Solan, Himachal Pradesh 173 221, India

Taranpreet Kaur – Department of Biotechnology, Government Mohindra College, Patiala, Punjab 147 001, India

Sebastian Sensale – Department of Aerospace and Mechanical Engineering, University of Notre Dame, Notre Dame, Indiana 46556-5637, United States

Zhangli Peng – Center for Bioinformatics and Quantitative Biology, Richard and Loan Hill Department of Bioengineering, University of Illinois, Chicago, Illinois 60612, United States

Deepak Kumar – School of Pharmaceutical Sciences, Shoolini University, Solan, Himachal Pradesh 173 221, India

Complete contact information is available at:

<https://pubs.acs.org/10.1021/acs.molpharmaceut.0c00730>

Notes

The authors declare no competing financial interest.

■ ACKNOWLEDGMENTS

The study was funded by Shoolini University, Solan, India. The authors would like to thank Prof. Kamal Dev for providing secondary antibodies. The authors also thank Venus Remedies, Everest Formulation Pvt. Ltd., SPB Pharma Pvt. Ltd., Cipla, and Roquette for gift samples. The authors also thank Ms. Shweta Kumari for her help in cell culture studies.

■ REFERENCES

- (1) Barzegar-Jalali, M.; Mohammadi, K.; Mohammadi, G.; Valizadeh, H.; Barzegar-Jalali, A.; Adibkia, K.; Nokhodchi, A. A correlative model to predict in vivo AUC for nanosystem drug delivery with release rate-limited absorption. *J. Pharm. Pharm. Sci.* **2012**, *15*, 583–591.
- (2) Date, A. A.; Hanes, J.; Ensign, L. M. Nanoparticles for oral delivery: Design, evaluation and state-of-the-art. *J. Controlled Release* **2016**, *240*, 504–526.
- (3) Modi, S.; Anderson, B. D. Determination of drug release kinetics from nanoparticles: Overcoming pitfalls of the dynamic dialysis method. *Mol. Pharmaceutics* **2013**, *10*, 3076–3089.
- (4) Shetty, Y.; Prabhu, P.; Prabhakar, B. Emerging vistas in theranostic medicine. *Int. J. Pharm.* **2019**, *558*, 29–42.
- (5) Li, S. Y.; Liu, L. H.; Jia, H. Z.; Qiu, W. X.; Rong, L.; Cheng, H.; Zhang, X. Z. A pH-responsive prodrug for real-time drug release monitoring and targeted cancer therapy. *Chem. Commun. (Cambridge, U. K.)* **2014**, *50*, 11852–11855.
- (6) Shen, T.; Zhang, Y.; Kirillov, A. M.; Cai, H.; Huang, K.; Liu, W.; Tang, Y. Two-photon sensitized hollow Gd₂O₃:Eu(3+) nano-

composites for real-time dual-mode imaging and monitoring of anticancer drug release. *Chem. Commun. (Cambridge, U. K.)* **2016**, *52*, 1447–1450.

(7) Weinstain, R.; Segal, E.; Satchi-Fainaro, R.; Shabat, D. Real-time monitoring of drug release. *Chem. Commun. (Cambridge, U. K.)* **2010**, *46*, 553–555.

(8) Wang, Z.; Wu, H.; Liu, P.; Zeng, F.; Wu, S. A self-immolative prodrug nanosystem capable of releasing a drug and a NIR reporter for in vivo imaging and therapy. *Biomaterials* **2017**, *139*, 139–150.

(9) Wang, C.; Wang, Z.; Zhao, X.; Yu, F.; Quan, Y.; Cheng, Y.; Yuan, H. DOX Loaded Aggregation-induced Emission Active Polymeric Nanoparticles as a Fluorescence Resonance Energy Transfer Traceable Drug Delivery System for Self-indicating Cancer Therapy. *Acta Biomater.* **2019**, *85*, 218–228.

(10) Dong, X.; Sun, Z.; Wang, X.; Zhu, D.; Liu, L.; Leng, X. Simultaneous monitoring of the drug release and antitumor effect of a novel drug delivery system-MWCNTs/DOX/TC. *Drug Delivery* **2017**, *24*, 143–151.

(11) Ye, M.; Wang, X.; Tang, J.; Guo, Z.; Shen, Y.; Tian, H.; Zhu, W. H. Dual-channel NIR activatable theranostic prodrug for in vivo spatiotemporal tracking thiol-triggered chemotherapy. *Chem. Sci.* **2016**, *7*, 4958–4965.

(12) Scarpa, E.; Bailey, J. L.; Janeczek, A. A.; Stumpf, P. S.; Johnston, A. H.; Oreffo, R. O.; Woo, Y. L.; Cheong, Y. C.; Evans, N. D.; Newman, T. A. Quantification of intracellular payload release from polymersome nanoparticles. *Sci. Rep.* **2016**, *6*, 29460.

(13) Viger, M. L.; Sheng, W.; McFearn, C. L.; Berezin, M. Y.; Almutairi, A. Application of time-resolved fluorescence for direct and continuous probing of release from polymeric delivery vehicles. *J. Controlled Release* **2013**, *171*, 308–314.

(14) Pramod, P. S.; Deshpande, N. U.; Jayakannan, M. Real-time drug release analysis of enzyme and pH responsive polysaccharide nanovesicles. *J. Phys. Chem. B* **2015**, *119*, 10511–10523.

(15) Dong, X.; Wei, C.; Liu, T.; Lv, F.; Qian, Z. Real-Time Fluorescence Tracking of Protoporphyrin Incorporated Thermosensitive Hydrogel and Its Drug Release in Vivo. *ACS Appl. Mater. Interfaces* **2016**, *8*, 5104–5113.

(16) Lai, J.; Shah, B. P.; Garfunkel, E.; Lee, K. B. Versatile fluorescence resonance energy transfer-based mesoporous silica nanoparticles for real-time monitoring of drug release. *ACS Nano* **2013**, *7*, 2741–2750.

(17) Li, H.; Lan, R.; Chan, C. F.; Jiang, L.; Dai, L.; Kwong, D. W.; Lam, M. H.; Wong, K. L. Real-time in situ monitoring via europium emission of the photo-release of antitumor cisplatin from a Eu-Pt complex. *Chem. Commun. (Cambridge, U. K.)* **2015**, *51*, 14022–14025.

(18) Li, H.; Harriss, B. I.; Phinikaridou, A.; Lacerda, S.; Ramniceanu, G.; Doan, B. T.; Ho, K. L.; Chan, C. F.; Lo, W. S.; Botnar, R. M.; Lan, R.; Richard, C.; Law, G. L.; Long, N. J.; Wong, K. L. Gadolinium and Platinum in Tandem: Real-time Multi-Modal Monitoring of Drug Delivery by MRI and Fluorescence Imaging. *Nanotheranostics* **2017**, *1*, 186–195.

(19) Kim, J.-W.; Kotagiri, N. Stealth nanotubes: strategies of shielding carbon nanotubes to evade opsonization and improve biodistribution. *Int. J. Nanomed.* **2014**, *9*, 85–105.

(20) Singh, R. P.; Das, M.; Thakare, V.; Jain, S. Functionalization Density Dependent Toxicity of Oxidized Multiwalled Carbon Nanotubes in a Murine Macrophage Cell Line. *Chem. Res. Toxicol.* **2012**, *25*, 2127–2137.

(21) Kotagiri, N.; Lee, J. S.; Kim, J. W. Selective pathogen targeting and macrophage evading carbon nanotubes through dextran sulfate coating and PEGylation for photothermal theranostics. *J. Biomed. Nanotechnol.* **2013**, *9*, 1008–1016.

(22) Abdollah, M. R.; Kalber, T.; Tolner, B.; Southern, P.; Bear, J. C.; Robson, M.; Pedley, R. B.; Parkin, I. P.; Pankhurst, Q. A.; Mulholland, P.; Chester, K. Prolonging the circulatory retention of SPIONs using dextran sulfate: in vivo tracking achieved by functionalisation with near-infrared dyes. *Faraday Discuss.* **2014**, *175*, 41–58.

(23) Wu, Z. S.; Liu, C. F.; Fu, B.; Chou, R. H.; Yu, C. Suramin blocks interaction between human FGFR1 and FGFR2 D2 domain and reduces downstream signaling activity. *Biochem. Biophys. Res. Commun.* **2016**, *477*, 861–867.

(24) Fujiuchi, S.; Ohsaki, Y.; Kikuchi, K. Suramin inhibits the growth of non-small-cell lung cancer cells that express the epidermal growth factor receptor. *Oncology* **2004**, *54*, 134–140.

(25) Koval, A.; Ahmed, K.; Katanaev, V. L. Inhibition of Wnt signalling and breast tumour growth by the multi-purpose drug suramin through suppression of heterotrimeric G proteins and Wnt endocytosis. *Biochem. J.* **2016**, *473*, 371–381.

(26) Ahmed, K.; Shaw, V. H.; Koval, A.; Katanaev, L. V. A Second WNT for Old Drugs: Drug Repositioning against WNT-Dependent Cancers. *Cancers* **2016**, *8*, 66.

(27) DiGiacomo, V.; de Opakua, A. I.; Papakonstantinou, M. P.; Nguyen, L. T.; Merino, N.; Blanco-Canosa, J. B.; Blanco, F. J.; Garcia-Marcos, M. The Gai-GIV binding interface is a druggable protein-protein interaction. *Sci. Rep.* **2017**, *7*, 8575.

(28) Berg, A.; Berg, T. A small-molecule screen identifies the antitrypanosomal agent suramin and analogues NF023 and NF449 as inhibitors of STAT5a/b. *Bioorg. Med. Chem. Lett.* **2017**, *27*, 3349–3352.

(29) Wang, X.; Li, L.; Guan, R.; Zhu, D.; Song, N.; Shen, L. Emodin Inhibits ATP-Induced Proliferation and Migration by Suppressing P2Y Receptors in Human Lung Adenocarcinoma Cells. *Cell. Physiol. Biochem.* **2017**, *44*, 1337–1351.

(30) Kakuguchi, W.; Nomura, T.; Kitamura, T.; Otsuguro, S.; Matsushita, K.; Sakaitani, M.; Maenaka, K.; Tei, K. Suramin, screened from an approved drug library, inhibits HuR functions and attenuates malignant phenotype of oral cancer cells. *Cancer Med.* **2018**, *7*, 6269–6280.

(31) Gan, Y.; Lu, J.; Yeung, B. Z.; Cottage, C. T.; Wientjes, M. G.; Au, J. L. S. Pharmacodynamics of telomerase inhibition and telomere shortening by noncytotoxic suramin. *AAPS J.* **2015**, *17*, 268–276.

(32) Ulus, G.; Koparal, A. T.; Baysal, K.; Yetik Anacak, G.; Karabay Yavaşoğlu, N. Ü. The anti-angiogenic potential of (±) gossypol in comparison to suramin. *Cytotechnology* **2018**, *70*, 1537–1550.

(33) Song, S.; Wientjes, M. G.; Walsh, C.; Au, J. L. Nontoxic doses of suramin enhance activity of paclitaxel against lung metastases. *Cancer Res.* **2001**, *61*, 6145–6150.

(34) Cheng, B.; Gao, F.; Maissy, E.; Xu, P. Repurposing suramin for the treatment of breast cancer lung metastasis with glycol chitosan-based nanoparticles. *Acta Biomater.* **2019**, *84*, 378–390.

(35) Wiedemar, N.; Hauser, D. A.; Mäser, P. 100 Years of Suramin. *Antimicrob. Agents Chemother.* **2020**, *64*, e01168–01119.

(36) Park, J.; Hwang, S. R.; Choi, J. U.; Alam, F.; Byun, Y. Self-assembled nanocomplex of PEGylated protamine and heparin–suramin conjugate for accumulation at the tumor site. *Int. J. Pharm.* **2018**, *535*, 38–46.

(37) Lv, M.; Li, X.; Huang, Y.; Wang, N.; Zhu, X.; Sun, J. Inhibition of fibrous dysplasia via blocking G α with suramin sodium loaded with an alendronate-conjugated polymeric drug delivery system. *Biomater. Sci.* **2016**, *4*, 1113–1122.

(38) Das, M.; Singh, R. P.; Datir, S. R.; Jain, S. Surface chemistry dependent “switch” regulates the trafficking and therapeutic performance of drug-loaded carbon nanotubes. *Bioconjugate Chem.* **2013**, *24*, 626–639.

(39) Singh, R. P.; Jain, S.; Ramarao, P. Surfactant-assisted dispersion of carbon nanotubes: mechanism of stabilization and biocompatibility of the surfactant. *J. Nanopart. Res.* **2013**, *15*, 1985.

(40) Kumar, S.; Das, M.; Singh, R. P.; Datir, S.; Chauhan, D. S.; Jain, S. Mathematical models for the oxidative functionalization of multiwalled carbon nanotubes. *Colloids Surf., A* **2013**, *419*, 156–165.

(41) WHO. *Suramin sodium (Suraminum natrium)*; World Health Organization: Geneva, 2018.

(42) Haghniaz, R.; Bhayani, K. R.; Umrani, R. D.; Paknikar, K. M. Dextran stabilized lanthanum strontium manganese oxide nanoparticles for magnetic resonance imaging. *RSC Adv.* **2013**, *3*, 18489–18497.

- (43) Eshghi, H.; Mirzaie, N.; Asoodeh, A. Synthesis of fluorescein aromatic esters in the presence of P2O5/SiO2 as catalyst and their hydrolysis studies in the presence of lipase. *Dyes Pigm.* **2011**, *89*, 120–126.
- (44) Waterhouse, A.; Bertoni, M.; Bienert, S.; Studer, G.; Tauriello, G.; Gumienny, R.; Heer, F. T.; de Beer, T. A. P.; Rempfer, C.; Bordoli, L.; Lepore, R.; Schwede, T. SWISS-MODEL: homology modelling of protein structures and complexes. *Nucleic Acids Res.* **2018**, *46*, W296–W303.
- (45) Krishnan, S.; Clementi, L.; Ren, J.; Papadopoulos, P.; Li, W. Design and Evaluation of Opal2: A Toolkit for Scientific Software as a Service. *2009 Congress on Services - I* **2009**, 709–716.
- (46) Zhang, Y.-L.; Keng, Y.-F.; Zhao, Y.; Wu, L.; Zhang, Z.-Y. Suramin Is an Active Site-directed, Reversible, and Tight-binding Inhibitor of Protein-tyrosine Phosphatases. *J. Biol. Chem.* **1998**, *273*, 12281–12287.
- (47) Guns, L.-A.; Monteagudo, S.; Kvasnytsia, M.; Kerckhofs, G.; Vandoreen, J.; Opendakker, G.; Lories, R. J.; Cailotto, F. Suramin increases cartilage proteoglycan accumulation in vitro and protects against joint damage triggered by papain injection in mouse knees in vivo. *RMD Open* **2017**, *3*, e000604–e000604.
- (48) Francia, V.; Reker-Smit, C.; Boel, G.; Salvati, A. Limits and challenges in using transport inhibitors to characterize how nano-sized drug carriers enter cells. *Nanomedicine* **2019**, *14*, 1533–1549.
- (49) Castagne, D.; Evrard, B.; Nusgens, B.; Piel, G. Effect of β -cyclodextrin and its derivatives on caveolae disruption, relationships with their cholesterol extraction capacities. *J. Inclusion Phenom. Mol. Recognit. Chem.* **2010**, *67*, 369–376.
- (50) Vainio, M. J.; Johnson, M. S. Generating Conformer Ensembles Using a Multiobjective Genetic Algorithm. *J. Chem. Inf. Model.* **2007**, *47*, 2462–2474.
- (51) Alomari, E.; Bruno, S.; Ronda, L.; Paredi, G.; Bettati, S.; Mozzarelli, A. Protein carbonylation detection methods: A comparison. *Data Brief* **2018**, *19*, 2215–2220.
- (52) Filyak, O. S.; Stoika, R. S. Comparative study of p53 expression in human carcinoma cell lines A549 and MCF7 under anticancer drug treatment. *Ukr Biokhim Zh (1999)* **2005**, *77*, 136–140.
- (53) Hulkower, K. I.; Herber, R. L. Cell migration and invasion assays as tools for drug discovery. *Pharmaceutics* **2011**, *3*, 107–124.
- (54) Rendon, B. E.; Roger, T.; Teneng, I.; Zhao, M.; Al-Abed, Y.; Calandra, T.; Mitchell, R. A. Regulation of Human Lung Adenocarcinoma Cell Migration and Invasion by Macrophage Migration Inhibitory Factor. *J. Biol. Chem.* **2007**, *282*, 29910–29918.
- (55) Wang, X.; Shen, Y.; Wang, S.; Li, S.; Zhang, W.; Liu, X.; Lai, L.; Pei, J.; Li, H. PharmMapper 2017 update: a web server for potential drug target identification with a comprehensive target pharmacophore database. *Nucleic Acids Res.* **2017**, *45*, W356–W360.
- (56) Liu, X.; Ouyang, S.; Yu, B.; Liu, Y.; Huang, K.; Gong, J.; Zheng, S.; Li, Z.; Li, H.; Jiang, H. PharmMapper server: a web server for potential drug target identification using pharmacophore mapping approach. *Nucleic Acids Res.* **2010**, *38*, W609–614.
- (57) Trott, O.; Olson, A. J. AutoDock Vina: improving the speed and accuracy of docking with a new scoring function, efficient optimization and multithreading. *J. Comput. Chem.* **2010**, *31*, 455–461.
- (58) Ren, J.; Williams, N.; Clementi, L.; Krishnan, S.; Li, W. W. Opal web services for biomedical applications. *Nucleic Acids Res.* **2010**, *38*, W724–731.
- (59) Puranen, J. S.; Vainio, M. J.; Johnson, M. S. Accurate conformation-dependent molecular electrostatic potentials for high-throughput in silico drug discovery. *J. Comput. Chem.* **2010**, *31*, 1722–1732.
- (60) Vainio, M. J.; Puranen, J. S.; Johnson, M. S. ShaEP: Molecular Overlay Based on Shape and Electrostatic Potential. *J. Chem. Inf. Model.* **2009**, *49*, 492–502.
- (61) Wang, X.; Pan, C.; Gong, J.; Liu, X.; Li, H. Enhancing the Enrichment of Pharmacophore-Based Target Prediction for the Polypharmacological Profiles of Drugs. *J. Chem. Inf. Model.* **2016**, *56*, 1175–1183.
- (62) Li, H.; Leung, K.-S.; Wong, M.-H.; Ballester, P. J. USR-VS: a web server for large-scale prospective virtual screening using ultrafast shape recognition techniques. *Nucleic Acids Res.* **2016**, *44*, W436–W441.
- (63) Ballester, P. J.; Richards, W. G. Ultrafast shape recognition to search compound databases for similar molecular shapes. *J. Comput. Chem.* **2007**, *28*, 1711–1723.
- (64) Schreyer, A. M.; Blundell, T. USRCAT: real-time ultrafast shape recognition with pharmacophoric constraints. *J. Cheminf.* **2012**, *4*, 27.
- (65) Jo, S.; Kim, T.; Iyer, V. G.; Im, W. CHARMM-GUI: A web-based graphical user interface for CHARMM. *J. Comput. Chem.* **2008**, *29*, 1859–1865.
- (66) Jo, S.; Cheng, X.; Islam, S. M.; Huang, L.; Rui, H.; Zhu, A.; Lee, H. S.; Qi, Y.; Han, W.; Vanommeslaeghe, K.; MacKerell, A. D.; Roux, B.; Im, W. Chapter Eight - CHARMM-GUI PDB Manipulator for Advanced Modeling and Simulations of Proteins Containing Non-standard Residues. *Adv. Protein Chem. Struct. Biol.* **2014**, *96*, 235–265.
- (67) Kim, S.; Lee, J.; Jo, S.; Brooks, C. L., III; Lee, H. S.; Im, W. CHARMM-GUI ligand reader and modeler for CHARMM force field generation of small molecules. *J. Comput. Chem.* **2017**, *38*, 1879–1886.
- (68) Humphrey, W.; Dalke, A.; Schulten, K. VMD: Visual molecular dynamics. *J. Mol. Graphics* **1996**, *14*, 33–38.
- (69) Lee, J.; Cheng, X.; Swails, J. M.; Yeom, M. S.; Eastman, P. K.; Lemkul, J. A.; Wei, S.; Buckner, J.; Jeong, J. C.; Qi, Y.; Jo, S.; Pande, V. S.; Case, D. A.; Brooks, C. L.; MacKerell, A. D.; Klauda, J. B.; Im, W. CHARMM-GUI Input Generator for NAMD, GROMACS, AMBER, OpenMM, and CHARMM/OpenMM Simulations Using the CHARMM36 Additive Force Field. *J. Chem. Theory Comput.* **2016**, *12*, 405–413.
- (70) Brooks, B. R.; Brooks, C. L., III; Mackerell, A. D., Jr.; Nilsson, L.; Petrella, R. J.; Roux, B.; Won, Y.; Archontis, G.; Bartels, C.; Boresch, S.; Cafisch, A.; Caves, L.; Cui, Q.; Dinner, A. R.; Feig, M.; Fischer, S.; Gao, J.; Hodoscek, M.; Im, W.; Kuczera, K.; Lazaridis, T.; Ma, J.; Ovchinnikov, V.; Paci, E.; Pastor, R. W.; Post, C. B.; Pu, J. Z.; Schaefer, M.; Tidor, B.; Venable, R. M.; Woodcock, H. L.; Wu, X.; Yang, W.; York, D. M.; Karplus, M. CHARMM: The biomolecular simulation program. *J. Comput. Chem.* **2009**, *30*, 1545–1614.
- (71) Phillips, J. C.; Braun, R.; Wang, W.; Gumbart, J.; Tajkhorshid, E.; Villa, E.; Chipot, C.; Skeel, R. D.; Kale, L.; Schulten, K. Scalable molecular dynamics with NAMD. *J. Comput. Chem.* **2005**, *26*, 1781–1802.
- (72) Yu, M.; Every, H. A.; Jiskoot, W.; Witkamp, G.-J.; Buijs, W. Molecular structure of dextran sulphate sodium in aqueous environment. *J. Mol. Struct.* **2018**, *1156*, 320–329.
- (73) Nadvorný, D.; Soares-Sobrinho, J. L.; de La Roca Soares, M. F.; Ribeiro, A. J.; Veiga, F.; Seabra, G. M. Molecular dynamics simulations reveal the influence of dextran sulfate in nanoparticle formation with calcium alginate to encapsulate insulin. *J. Biomol. Struct. Dyn.* **2018**, *36*, 1255–1260.
- (74) Jo, S.; Song, K. C.; Desaire, H.; MacKerell, A. D., Jr.; Im, W. Glycan reader: Automated sugar identification and simulation preparation for carbohydrates and glycoproteins. *J. Comput. Chem.* **2011**, *32*, 3135–3141.
- (75) Park, S.-J.; Lee, J.; Patel, D. S.; Ma, H.; Lee, H. S.; Jo, S.; Im, W. Glycan Reader is improved to recognize most sugar types and chemical modifications in the Protein Data Bank. *Bioinformatics* **2017**, *33*, 3051–3057.
- (76) Park, S.-J.; Lee, J.; Qi, Y.; Kern, N. R.; Lee, H. S.; Jo, S.; Joung, I.; Joo, K.; Lee, J.; Im, W. CHARMM-GUI Glycan Modeler for modeling and simulation of carbohydrates and glycoconjugates. *Glycobiology* **2019**, *29*, 320–331.
- (77) Cui, X.; Wan, B.; Yang, Y.; Ren, X.; Guo, L.-H. Length effects on the dynamic process of cellular uptake and exocytosis of single-walled carbon nanotubes in murine macrophage cells. *Sci. Rep.* **2017**, *7*, 1518.

- (78) Duan, Y.; Liu, M.; Sun, W.; Wang, M.; Liu, S.; Li, Q. X. Recent Progress on Synthesis of Fluorescein Probes. *Mini-Rev. Org. Chem.* **2009**, *6*, 35–43.
- (79) Csoka, I.; Pallagi, E.; Paal, T. L. Extension of quality-by-design concept to the early development phase of pharmaceutical R&D processes. *Drug Discovery Today* **2018**, *23*, 1340–1343.
- (80) Fukuda, I. M.; Pinto, C. F. F.; Moreira, C. d. S.; Saviano, A. M.; Lourenço, F. R. Design of Experiments (DoE) applied to Pharmaceutical and Analytical Quality by Design (QbD). *Brazilian Journal of Pharmaceutical Sciences* **2018**, *54*, 1.
- (81) Rawal, M.; Singh, A.; Amiji, M. M. Quality-by-Design Concepts to Improve Nanotechnology-Based Drug Development. *Pharm. Res.* **2019**, *36*, 153.
- (82) Gurunathan, S.; Kang, M. H.; Qasim, M.; Kim, J. H. Nanoparticle-Mediated Combination Therapy: Two-in-One Approach for Cancer. *Int. J. Mol. Sci.* **2018**, *19*, 3264.
- (83) Huang, W.-Y.; Yang, P.-M.; Chang, Y.-F.; Marquez, V. E.; Chen, C.-C. Methotrexate induces apoptosis through p53/p21-dependent pathway and increases E-cadherin expression through downregulation of HDAC/EZH2. *Biochem. Pharmacol.* **2011**, *81*, 510–517.
- (84) Fischer, M. Census and evaluation of p53 target genes. *Oncogene* **2017**, *36*, 3943.
- (85) Hampp, S.; Kiessling, T.; Buechle, K.; Mansilla, S. F.; Thomale, J.; Rall, M.; Ahn, J.; Pospiech, H.; Gottifredi, V.; Wiesmüller, L. DNA damage tolerance pathway involving DNA polymerase ι and the tumor suppressor p53 regulates DNA replication fork progression. *Proc. Natl. Acad. Sci. U. S. A.* **2016**, *113*, E4311.
- (86) Shannahan, J. H.; Brown, J. M.; Chen, R.; Ke, P. C.; Lai, X.; Mitra, S.; Witzmann, F. A. Comparison of nanotube-protein corona composition in cell culture media. *Small* **2013**, *9*, 2171–2181.
- (87) De Paoli, S. H.; Diduch, L. L.; Tegegn, T. Z.; Orecna, M.; Strader, M. B.; Karnaukhova, E.; Bonevich, J. E.; Holada, K.; Simak, J. The effect of protein corona composition on the interaction of carbon nanotubes with human blood platelets. *Biomaterials* **2014**, *35*, 6182–6194.
- (88) Xu, Y.; Jin, X.; Huang, Y.; Wang, J.; Wang, X.; Wang, H. Dextran sulfate inhibition on human gastric cancer cells invasion, migration and epithelial-mesenchymal transformation. *Oncol. Lett.* **2018**, *16*, 5041–5049.
- (89) Xu, Y.; Jin, X.; Huang, Y.; Dong, J.; Wang, H.; Wang, X.; Cao, X. Inhibition of peritoneal metastasis of human gastric cancer cells by dextran sulphate through the reduction in HIF-1 α and ITG β 1 expression. *Oncol. Rep.* **2016**, *35*, 2624–2634.
- (90) Yang, M.; Wang, N.; Li, W.; Li, H.; Zhao, Y.; Yao, S.; Chen, W. Therapeutic effects of scavenger receptor MARCO ligand on silica-induced pulmonary fibrosis in rats. *Toxicol. Lett.* **2019**, *311*, 1–10.
- (91) Verbij, F. C.; Sorvillo, N.; Kaijen, P. H. P.; Hrdinova, J.; Peyron, I.; Fijnheer, R.; Ten Brinke, A.; Meijer, A. B.; van Alphen, F. P. J.; van den Berg, T. K.; Graversen, J. J. H.; Moestrup, S. K.; Voorberg, J. The class I scavenger receptor CD163 promotes internalization of ADAMTS13 by macrophages. *Blood Adv.* **2017**, *1*, 293–305.
- (92) Liu, H.; Qin, Y.; Zhai, D.; Zhang, Q.; Gu, J.; Tang, Y.; Yang, J.; Li, K.; Yang, L.; Chen, S.; Zhong, W.; Meng, J.; Liu, Y.; Sun, T.; Yang, C. Antimalarial drug pyrimethamine plays a dual role in anti-tumor proliferation and metastasis through targeting DHFR and TP. *Molecular Cancer Therapeutics* **2019**, 541.
- (93) Ohbayashi, M.; Kubota, S.; Kawase, A.; Kohyama, N.; Kobayashi, Y.; Yamamoto, T. Involvement of epithelial-mesenchymal transition in methotrexate-induced pulmonary fibrosis. *J. Toxicol. Sci.* **2014**, *39*, 319–330.
- (94) Lin, Y.; Xu, J.; Lan, H. Tumor-associated macrophages in tumor metastasis: biological roles and clinical therapeutic applications. *J. Hematol. Oncol.* **2019**, *12*, 76.
- (95) Pathria, P.; Louis, T. L.; Varner, J. A. Targeting Tumor-Associated Macrophages in Cancer. *Trends Immunol.* **2019**, *40*, 310–327.
- (96) Yu, X.; Guo, C.; Fisher, P. B.; Subject, J. R.; Wang, X.-Y. Chapter Nine - Scavenger Receptors: Emerging Roles in Cancer Biology and Immunology. *Adv. Cancer Res.* **2015**, *128*, 309–364.
- (97) Georgoudaki, A.-M.; Prokopec, K.; Boura, V. F.; Hellqvist, E.; Sohn, S.; Östling, J.; Harris, R. A.; Rantalainen, M.; Klevebring, D.; Sund, M.; Fuxe, J.; Rolny, C.; Li, F.; Ravetch, J. V.; C.I. Karlsson, M. Reprogramming tumor-associated macrophages by antibody targeting inhibits cancer progression and metastasis. *Cell Rep.* **2016**, *15*, 2000–2011.
- (98) Neyen, C.; Pluddemann, A.; Mukhopadhyay, S.; Maniati, E.; Bossard, M.; Gordon, S.; Hagemann, T. Macrophage Scavenger Receptor A Promotes Tumor Progression in Murine Models of Ovarian and Pancreatic Cancer. *J. Immunol.* **2013**, *190*, 3798–3805.
- (99) Kotagiri, N.; Kim, J.-W. Carbon Nanotubes Fed on “Carbs”: Coating of Single-Walled Carbon Nanotubes by Dextran Sulfate. *Macromol. Biosci.* **2010**, *10*, 231–238.
- (100) Azari, A.; Nabizadeh, R.; Nasser, S.; Mahvi, A. H.; Mesdaghinia, A. R. Comprehensive systematic review and meta-analysis of dyes adsorption by carbon-based adsorbent materials: Classification and analysis of last decade studies. *Chemosphere* **2020**, *250*, 126238.
- (101) Awad, A. M.; Jalab, R.; Benamor, A.; Nasser, M. S.; Ba-Abbad, M. M.; El-Naas, M.; Mohammad, A. W. Adsorption of organic pollutants by nanomaterial-based adsorbents: An overview. *J. Mol. Liq.* **2020**, *301*, 112335.
- (102) Sensale, S.; Wang, C.; Chang, H. C. Resistive amplitude fingerprints during translocation of linear molecules through charged solid-state nanopores. *J. Chem. Phys.* **2020**, *153*, No. 035102.
- (103) Yang, M.; Ding, J.; Feng, X.; Chang, F.; Wang, Y.; Gao, Z.; Zhuang, X.; Chen, X. Scavenger Receptor-Mediated Targeted Treatment of Collagen-Induced Arthritis by Dextran Sulfate-Methotrexate Prodrug. *Theranostics* **2017**, *7*, 97–105.